THESIS FOR THE DEGREE OF DOCTOR OF PHILOSOPHY

Methane oxidation over palladium oxide: From electronic structure to catalytic conversion

MAXIME VAN DEN BOSSCHE

CHALMERS

Department of Physics
Chalmers University of Technology
Gothenburg, Sweden 2017

Methane oxidation over palladium oxide:
From electronic structure to catalytic conversion
MAXIME VAN DEN BOSSCHE
ISBN 978-91-7597-545-0

Doktorsavhandlingar vid Chalmers tekniska högskola
Ny serie nr 4226
ISSN 0346-718X

Department of Physics
Chalmers University of Technology
SE-412 96 Gothenburg
Sweden
Telephone: +46 (0)31-772 1000

Cover:
Ball-and-stick model of CH_4 dissociation over the PdO(101) surface. The isosurface represents a maximally localized Wannier orbital showing the hybridization between the C-H σ-bond and a Pd d_{z^2} orbital. The atomic colour codes are:
gray – Pd, *red* – O, *black* – C, *white* – H.

Printed at Chalmers Reproservice
Gothenburg, Sweden 2017

Methane oxidation over palladium oxide:
From electronic structure to catalytic conversion

Maxime Van den Bossche
Department of Physics
Chalmers University of Technology

Abstract

Understanding how catalysts work down to the atomic level can provide ways to improve chemical processes on which our contemporary economy is heavily reliant. The oxidation of methane is one such example, which is important from an environmental point of view. Methane is a potent greenhouse gas and natural and biogas vehicles need efficient catalysts to prevent slip of uncombusted fuel into the exhaust. Commercial catalysts for methane oxidation are often based on palladium or platinum. Metallic palladium, however, is easily converted to palladium oxide when the engine is operated at oxygen rich conditions.
In this thesis, various aspects of complete methane oxidation over PdO(101) are investigated with computational methods based on density functional theory (DFT). PdO(101) is the active surface for methane oxidation, and firstly, the reaction intermediates CO and H are studied in detail. Possible pathways for H_2 adsorption, dissociation and eventual water formation are investigated, in connection to core-level spectroscopy experiments. Similarly, the adsorption configurations for carbon monoxide on clean and oxidized palladium are examined with a combination of DFT calculations, core-level and infrared spectroscopy.
Secondly, a detailed kinetic model is constructed that describes the catalytic conversion of CH_4 to CO_2 and H_2O over PdO(101). This is done in a first-principles microkinetics framework, where the kinetic parameters are obtained by applying density functional and transition state theory. The kinetic model provides a fundamental understanding of findings from reactor experiments, such as the rate limiting steps and poisoning behaviour, and shows qualitatively different behaviour of adsorbates on oxide as compared to metal surfaces.
Lastly, limitations of the commonly used class of generalized gradient functionals are illustrated in the computation of several properties of adsorbates on metal oxide surfaces. These include core-level shifts and thermodynamic and reactive properties of adsorbates on the PdO(101) surface. Similarly, the description of several molecular and cooperative adsorption processes are also found to be sensitive to the applied exchange-correlation functional on the BaO(100), TiO_2(110) and CeO_2(111) surfaces.

Keywords: heterogeneous catalysis, methane oxidation, palladium oxide, PdO(101), density functional theory, microkinetic modelling, core-level spectroscopy.

List of Publications

This thesis is based on the following appended publications:

I. Dissociative adsorption of hydrogen on PdO(101) studied by HRCLS and DFT
N. M. Martin, M. Van den Bossche, H. Grönbeck, C. Hakanoglu, J. Gustafson, S. Blomberg, M. A. Arman, A. Antony, R. Rai, A. Asthagiri, J. F. Weaver, and E. Lundgren
J. Phys. Chem. C, **117** (2013), 13510-13519

II. CO adsorption on clean and oxidized Pd(111)
N. M. Martin, M. Van den Bossche, H. Grönbeck, C. Hakanoglu, F. Zhang, T. Li, J. Gustafson, J. F. Weaver, and E. Lundgren
J. Phys. Chem. C, **118** (2014), 1118-1128

III. Intrinsic ligand effect governing the catalytic activity of Pd oxide thin films
N. M. Martin, M. Van den Bossche, A. Hellman, H. Grönbeck, C. Hakanoglu, J. Gustafson, S. Blomberg, N. Johansson, Z. Liu, S. Axnanda, J. F. Weaver, and E. Lundgren
ACS Catal., **4** (2014), 3330-3334

IV. Methane oxidation over PdO(101) revealed by first-principles kinetic modeling
M. Van den Bossche and H. Grönbeck
J. Am. Chem. Soc., **137** (2015), 12035-12044

V. Adsorbate pairing on oxide surfaces: influence on reactivity and dependence on the oxide, adsorbate pair and density functional
M. Van den Bossche and H. Grönbeck
Submitted to J. Phys. Chem. C

VI. Reversed hysteresis during CO oxidation over $Pd_{75}Ag_{25}$(100)
V. R. Fernandes, M. Van den Bossche, J. Knudsen, M. H. Farstad, J. Gustafson, H. J. Venvik, H. Grönbeck, and A. Borg
ACS Catal., **6** (2016), 4154-4161

VII. Effects of non-local exchange on core level shifts for gas-phase and adsorbed molecules
M. Van den Bossche, N. M. Martin, J. Gustafson, C. Hakanoglu, J. F. Weaver, E. Lundgren, and H. Grönbeck
J. Chem. Phys., **141** (2014), 034706

Related publications not included in this thesis:

Trends in adsorbate induced core level shifts
V. Nilsson, M. Van den Bossche, A. Hellman, and H. Grönbeck
Surf. Sci., **640** (2015), 59-64

My contributions to the publications

Paper I
I performed all the calculations and co-authored the theoretical part of the paper.

Paper II
I performed all the calculations and co-authored the theoretical part of the paper.

Paper III
I performed all the calculations and co-authored the theoretical part of the paper.

Paper IV
I performed all the calculations, wrote the first draft and finalized the paper together with my co-author.

Paper V
I performed all the calculations, wrote the first draft and finalized the paper together with my co-author.

Paper VI
I performed all the calculations and co-authored the theoretical part of the paper.

Paper VII
I performed all the calculations, wrote the first draft and finalized the paper together with my co-authors.

Contents

Chapter 1

Introduction

Our society faces challenges in all areas of sustainable development [1]. One of the most pressing environmental issues is the release of pollutants by human activity. Greenhouse gas (GHG) emissions are suspected to be the main cause for the observed global warming of the planet. A number of initiatives therefore aim to reduce these emissions. One example is the EU 2020 strategy [2], where one of the targets is to lower the GHG emissions by at least 20% by 2020 (compared to 1990).

Important anthropogenic GHGs include carbon dioxide, methane, chlorofluorocarbons and nitrous oxide [3]. While emissions of non-carbon dioxide GHGs, such as methane, are much lower than that of carbon dioxide, their contributions to the greenhouse effect are considerable due to their higher global warming potential (about ten times that of carbon dioxide on a molar basis for methane [4]). For methane, emission sources include agriculture, waste treatment, oil, gas and coal extraction and fuel combustion [5]. It is preferable to oxidize methane into carbon dioxide, which is a less harmful pollutant.

The contribution of methane emissions from the transportation and energy sector is expected to grow due to the increasing use of methane-based fuels, as an alternative to traditional fossil fuels [6]. The main reasons for this increase are (i) lower carbon dioxide emissions per unit of energy generated, (ii) lower particulate emissions compared to traditional fuels, (iii) the existence of large reserves of natural gas, and (iv) the possibility of using environmentally friendly biogas. Regarding the transportation sector, natural gas vehicles are especially common in Asian and South American countries [7]. A more nearby example is the GoBiGas project [8] in Göteborg, where the aim is to produce biogas through gasification of biomass, so as to promote the use of biogas vehicles in the region. In the energy sector, natural and biogas power stations are on the rise, in part because efficient gas turbines are a common choice in high efficiency combined heat and power generation cycles [9].

Combustion engines running on methane-rich fuels are plagued by unburned methane slipping into the exhaust. A similar issue is present in catalytic combustors used in gas turbines to burn the fuel at more moderate temperatures, so as to reduce e.g. NO_x emissions [6]. To avoid increasing the temperature in order to burn the remaining methane,

a catalyst is generally used to speed up the oxidation.

Commercial catalysts are based on precious transition metals such as palladium or platinum [6]. These catalytically active materials are present as nanometer-sized particles dispersed on the surface of a porous support, such as alumina, silica or ceria. The methane and oxygen reactants that are present in the gas stream adsorb on the catalyst surface, where the subsequent chemical reactions between them take place. Aside from the 'engineering' problems in optimizing the mass and heat flow through a catalytic reactor, there is still considerable room to improve the actual 'chemistry' occurring on the catalyst. On one hand, it is desirable to increase the intrinsic activity of these catalysts, so that more of the methane is being converted. On the other hand, decreasing (or even eliminating) the active metal content allows a more efficient use of the limited precious metal reserves on Earth.

1.1 Unravelling surface reactions

In order to improve the catalytic activity and selectivity, it is beneficial to start with understanding of how the current catalysts are able to carry out the chemical process. Insights in how technical catalysts work can however be hard to acquire. The catalysts can adopt various structures and compositions and are exposed to complex feed streams. One successful approach to this problem has been to reduce the catalyst to its essential part and to thereby identify and investigate the catalytically active material itself, without the support. A further disentanglement can be achieved by separately studying the different ideal crystal surfaces of the material under consideration. In order to perform detailed experiments, such as X-ray spectroscopy, also the pressure needs to be much lower than atmospheric pressure. Conventional setups require high vacuum conditions (around 10^{-8} 10^{-7} millibar), while advanced instruments allow total pressures up to 1 millibar.

Both the simplification of the material and the lowering of the pressures lead to a certain discrepancy between the studied material and the technical catalysts. This is called the 'materials gap' and 'pressure gap', respectively. However, once a firm understanding has been obtained on this level, the complexity can be gradually brought back in. Surface defects can for example be included, as well as effects of the support material and the behaviour at relevant pressures.

Computational physics/chemistry can have different roles to play in this process of understanding and improving catalytic materials. Electronic structure calculations can offer access to (in principle) all properties of a material starting from 'first principles', i.e. from fundamental physical theories. This means that theoretical predictions can aid

the interpretation of measurements. Additionally, some properties can be more easily tackled from a theoretical point of view. Surface energies and detailed reaction kinetics are examples of such properties. Thirdly, a first-principles viewpoint has a high potential in the rational design of new, as yet unsynthesized catalytic materials.

1.2 Objectives

The general aim of this thesis is to attain a more fundamental, molecular-level understanding of methane oxidation on transition metals and their oxides, especially palladium oxide, using theoretical methods. Additionally, the total oxidation of methane can serve as a model system for the oxidation of more complex hydrocarbons and can also yield insights regarding partial oxidation reactions, e.g. from methane to methanol. The different elements of this thesis are represented in Figure 1.1.

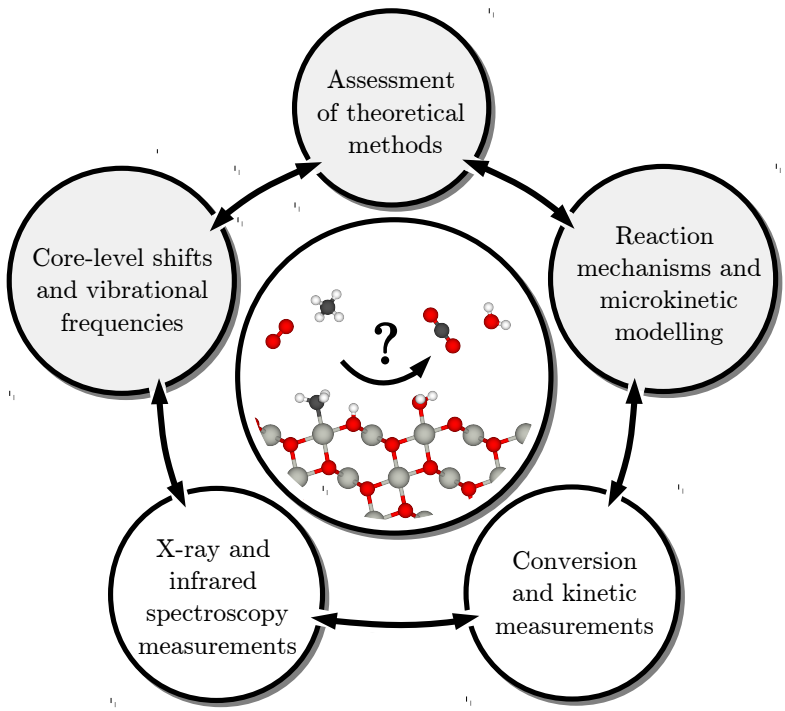

Figure 1.1: Schematic representation of the different elements used in this thesis to study methane oxidation over palladium oxide.

Several aspects of methane oxidation have been investigated during the course of this work. The approach has been to build up the complexity in steps, with continued feedback between computations and experiments. On one hand, density functional theory studies were performed to address the elementary processes of methane oxidation. These are the interaction of carbon monoxide and hydrogen with the oxidized palladium surfaces, in connection to experimental spectroscopic measurements. Secondly, a detailed kinetic model was built for the complete conversion of methane over the PdO(101) surface, providing a more fundamental understanding of experimental reactor data. Lastly, also the accuracy of the employed computational methods has been investigated.

Chapter 2

Electronic structure

> *"Nature isn't classical, dammit, and if you want to make a simulation of nature, you'd better make it quantum mechanical, and by golly it's a wonderful problem, because it doesn't look so easy.*
>
> – Richard P. Feynman [10]

Although the above statement was originally made in the context of quantum computing, it also sounds appropriate when applying quantum mechanics to chemical problems. Solids and molecules are made up of electrons and nuclei, which can, in principle, be exactly described by a many-body wave function obtained by solving the Schrödinger (or Dirac) wave equation. The quantum many-body problem can, however, only be solved analytically in the case of one-electron systems and also exact numerical solutions are hard to come by. This is due to the fact that the many-body wave function must not only reflect the Coulomb interactions between the particles, but must also obey antisymmetry with respect to the exchange of two particles.

As a consequence, different approaches have been advanced to find an approximate solution to the Schrödinger equation for many-particle systems. The two most widely used families of methods are those based on Hartree-Fock theory and Density Functional Theory (DFT). For problems involving surfaces and with structural models including several tens of atoms (up to around a thousand atoms), DFT is frequently the method of choice.

The following sections give an introduction to DFT and an example of how it can be implemented in a practical computer code. First, however, the Born-Oppenheimer and non-relativistic approximations will be discussed. While DFT is not bound by these approximations, they are common in the study of chemical problems.

2.1 The electronic Hamiltonian

In the Born-Oppenheimer approximation, the electrons are assumed to stay in the same adiabatic eigenstate when the coordinates of the nuclei are changed. This means that the

electronic and nucleic motions are considered to be decoupled and that the many-body wave function can be written as a product of an electronic and a nucleic wave function. The electronic wave function obeys an electronic Schrödinger equation, with an external potential that depends on the instantaneous positions of the nuclei. In turn, the potential energy in the nucleic equation of motion depends on the electronic eigenstate (e.g. the ground state). This assumption is typically valid except if the nuclei are moving fast and the electronic energy levels are closely spaced. In other words, the nuclei are stationary from the electrons' point of view and one can focus on solving the electronic Schrödinger equation, for given positions of the nuclei.

Another approximation is that the electrons are treated as non-relativistic particles, which is justified as long as they do not reach relativistic speeds. This is commonly the case for the valence electrons. Core electrons, however, require a relativistic treatment at least for elements starting from the fourth row [11]. A relativistic treatment of the core electrons is important as this will affect the electronic spectrum also in the valence. A fully relativistic method also includes spin-orbit coupling.

Within a non-relativistic treatment assuming the Born-Oppenheimer approximation, the time-independent electronic wave function $\Psi(\mathbf{r}_1, \ldots, \mathbf{r}_N, \sigma_1, \ldots, \sigma_N)$ for a set of N electrons in the presence of M nuclei obeys the Schrödinger equation:

$$E\Psi(\mathbf{r}_1, \ldots, \mathbf{r}_N, \sigma_1, \ldots, \sigma_N) = H\Psi(\mathbf{r}_1, \ldots, \mathbf{r}_N, \sigma_1, \ldots, \sigma_N). \tag{2.1}$$

The symbol $\mathbf{r}$ denotes the spatial coordinates and σ refers to the spin coordinate ($\pm\frac{1}{2}$ in a collinear spin treatment). The Hamiltonian H is the sum of kinetic and potential energy operators (in atomic units):

$$H = T + V_{\text{ext}} + V_{\text{el}}, \tag{2.2}$$

$$T = -\frac{1}{2}\sum_{i}^{N} \nabla_i^2, \tag{2.3}$$

$$V_{\text{ext}} = \sum_{i}^{N}\sum_{j}^{M} \frac{Z_j}{|\mathbf{R}_j - \mathbf{r}_i|}, \tag{2.4}$$

$$V_{\text{el}} = \sum_{i}^{N}\sum_{j<i} \frac{1}{|\mathbf{r}_j - \mathbf{r}_i|}. \tag{2.5}$$

Here, the external potential V_{ext} represents the Coulomb attraction of the electrons to the nuclei and V_{el} the potential arising from the Coulomb repulsion between the electrons.

2.2 Density functional theory

Already in 1927 alternative approaches to the Schrödinger equation were formulated by Thomas and Fermi [13, 14] that relied on the electron *density* as the central variable, rather than the intractable many-body wave function. However, these methods lacked a rigorous basis until Hohenberg and Kohn [15] showed in 1964 that there exists a functional F that maps the electron density function $\rho(\mathbf{r})$ to the electronic energy E:

$$E = F\left[\rho(\mathbf{r})\right] = F\left[\rho\right]. \tag{2.6}$$

If contributions from the external potential and from the classical Coulomb ('Hartree') potential are separated from F, one obtains:

$$E = E_{\text{ext}}\left[\rho\right] + E_{\text{Hartree}}\left[\rho\right] + G\left[\rho\right], \tag{2.7}$$

$$E_{\text{ext}}\left[\rho\right] = \int V_{\text{ext}}(\mathbf{r})\rho(\mathbf{r})d\mathbf{r}, \tag{2.8}$$

$$V_{\text{ext}}(\mathbf{r}) = \sum_{j}^{M} \frac{Z_j}{|\mathbf{R}_j - \mathbf{r}|}, \tag{2.9}$$

$$E_{\text{Hartree}}\left[\rho\right] = \frac{1}{2}\int V_{\text{Hartree}}(\mathbf{r})\rho(\mathbf{r})d\mathbf{r}, \tag{2.10}$$

$$V_{\text{Hartree}}(\mathbf{r}) = \int \frac{\rho(\mathbf{r}')}{|\mathbf{r} - \mathbf{r}'|}d\mathbf{r}'. \tag{2.11}$$

The Hohenberg-Kohn theorem implies that we can use the density $\rho(\mathbf{r})$ instead of the many-body wave function $\Psi(\mathbf{r}_1, \ldots, \mathbf{r}_N, \sigma_1, \ldots, \sigma_N)$ to obtain electronic properties. While this approach is potentially much more efficient, the exact form of the functional G is unknown and will probably remain so.

One particularly successful approach to use the result by Hohenberg and Kohn is that by Kohn and Sham [16], which is largely the reason for the wide popularity of DFT schemes. They showed that the ground state density and energy can be obtained by solving a set of one-electron equations instead of solving the many-electron problem. Kohn-Sham theory assumes that the total electron density can be represented as the sum of the orbital densities of non-interacting electrons:

$$\rho(\mathbf{r}) = \sum_{i}^{N} |\psi_i(\mathbf{r})|^2. \tag{2.12}$$

Then, the kinetic energy functional for the non-interacting particles can be separated from $G[\rho]$:

$$G[\rho] = T_{\text{non-int}}[\rho] + E_{\text{xc}}[\rho], \tag{2.13}$$

$$T_{\text{non-int}}[\rho] = -\frac{1}{2}\sum_{i}^{N} \langle \psi_i | \nabla^2 | \psi_i \rangle . \tag{2.14}$$

The exchange-correlation functional E_{xc} is usually constructed to depend on the separate spin densities $\rho_\uparrow$ and $\rho_\downarrow$ rather than the total density ρ.

It may seem peculiar to reintroduce the orbitals in a formalism based on the density, as it noticeably increases the complexity compared to using the total electron density alone. With this approach, however, the kinetic energy is well described. This is critical in e.g. covalent bonding and is a major reason for the failures of Thomas-Fermi theory [17].

The true electron density is obtained if the independent particles obey the single-particle Kohn-Sham equations. These equations are given by:

$$\left(-\frac{1}{2}\nabla^2 + v_{\text{eff}}(\mathbf{r},\sigma)\right)\psi_i(\mathbf{r},\sigma) = \epsilon_i \psi_i(\mathbf{r},\sigma). \tag{2.15}$$

All (same-spin) particles move in the same local effective potential $v_{\text{eff}}(\mathbf{r},\sigma)$ determined as:

$$v_{\text{eff}}(\mathbf{r},\sigma) = v_{\text{ext}}(\mathbf{r}) + v_{\text{Hartree}}(\mathbf{r}) + v_{\text{xc}}(\mathbf{r},\sigma), \tag{2.16}$$

$$v_{\text{xc}}(\mathbf{r},\sigma) = \frac{\partial E_{\text{xc}}[\rho_\downarrow, \rho_\uparrow]}{\partial \rho(\mathbf{r},\sigma)}. \tag{2.17}$$

The set of Kohn-Sham equations is to be solved self-consistently (see subsection 2.3.3), under the constraint that the integrated density equals the number of electrons N. The total energy in the Kohn-Sham approach equals:

$$E_{\text{tot}} = T_{\text{non-int}} + E_{\text{ext}} + E_{\text{Hartree}} + E_{\text{xc}}. \tag{2.18}$$

Due to their auxiliary character, the individual one-electron orbitals and eigenvalues do not have a rigorous meaning. The eigenvalues do not correspond to an ionization potential, as the eigenvalues in Hartree-Fock theory (Koopman's theorem [18]). The exception is the eigenvalue of the highest occupied state in a finite system, which (with the exact functional) corresponds to the negative of the first electronically relaxed ionization

potential [19]. Likewise, the Kohn-Sham band gap does not necessarily correspond to the gap measured experimentally [20]. Another consequence of reformulating the many-body problem in terms of one-electron orbitals is that the total energy of the interacting system is not simply equal to the sum of the Kohn-Sham eigenvalues, but rather:

$$E_{\text{tot}} = \sum_{i}^{N} \epsilon_i - E_{\text{Hartree}}[\rho] + E_{\text{xc}}[\rho_\downarrow, \rho_\uparrow] - \int \rho(\mathbf{r}) v_{\text{xc}}(\mathbf{r}) d\mathbf{r}. \tag{2.19}$$

Empirically, however, it is known that the orbital shapes and density of states can be used to analyze chemical bonding [21, 22]. Even more chemically meaningful representations can be acquired by unitary transformation to maximally localized orbitals [23].

It is clear that the potential benefits of the Kohn-Sham approach are huge, as the independent-particle problem is much easier to solve than the original many-body problem. The difficulties instead lie in the exchange-correlation functional E_{xc}, which is the term where all the complicated quantities are hidden. Effects that E_{xc} should capture are:

(i) Owing to the fermionic nature of the electron, the many-body wavefunction must change sign when two electrons are exchanged. This is generally referred to as 'electronic exchange'. This antisymmetry requirement ultimately results in a larger spatial separation between same-spin electrons, which results in a lowering of the electronic repulsion. Moreover, the nuclear charge is in this way less effectively screened.

(ii) Other effects are also present from the purely classical interactions between the electrons. The effect of 'instantaneous' Coulomb correlation, for example, is not captured by the mean-field character of the Hartree energy expression.

(iii) The self-interaction in the Hartree term needs to be corrected by E_{xc}. The Hartree energy namely contains artificial interactions of the electrons with themselves, which is clearly visible in the case of one electron where the Hartree energy is non-zero.

(iv) Lastly, E_{xc} should also take into account the difference in kinetic energy of the interacting and non-interacting electrons.

As with the Hohenberg-Kohn functional, the exact form of the Kohn-Sham exchange-correlation functional is likely to remain unknown. The strength of Kohn-Sham DFT lies in the fact that there exist computationally tractable approximations to the exchange-correlation functional which can yield quite accurate results. The development of these

approximations has been guided, in part, by a series of constraints [24, 25] that apply to the exact functional.

A very useful analysis, in this regard, is obtained through what is called the 'adiabatic connection' [26–30]. Following the fact that the exchange-correlation functional maps the fully interacting system to a non-interacting one, it can be shown that the exchange-correlation energy can be written as the coupling-constant integral:

$$E_{\rm xc} = \int_0^1 E_{{\rm xc},\lambda} d\lambda. \tag{2.20}$$

$E_{{\rm xc},\lambda}$ is the exchange-correlation energy for a system where the Coulomb interaction has been scaled by the coupling-constant λ and where the external potential is modified such that the ground state density is the same as in the fully interacting case. The exchange-correlation energy can be decomposed into separate exchange and correlation contributions, corresponding to the non-interacting ($\lambda = 0$) limit and the coupling-constant integration ($\lambda = 0 \rightarrow 1$), respectively.

If the non-interacting Kohn-Sham wave function can be represented as a single Slater determinant, the exchange energy is exactly given by the Hartree-Fock (HF) exchange integral [29]:

$$E_{{\rm xc},\lambda=0} = E_{\rm x}^{\rm HF} = -\frac{1}{2} \sum_{i \neq j}^{occup.} \iint \frac{\psi_i^*(\mathbf{r})\psi_j(\mathbf{r})\psi_j^*(\mathbf{r}')\psi_i(\mathbf{r}')}{|\mathbf{r}-\mathbf{r}'|} d\mathbf{r} d\mathbf{r}'. \tag{2.21}$$

The full exchange-correlation energy can be shown to correspond to the interaction of the density with a (coupling-constant-averaged) positively charged hole $h_{\rm xc}$ created around each electron as a result of Pauli and Coulomb repulsion:

$$E_{\rm xc} = \frac{1}{2} \iint \frac{\rho(\mathbf{r})}{|\mathbf{r}-\mathbf{r}'|} \left(\int_0^1 h_{{\rm xc},\lambda}(\mathbf{r},\mathbf{r}')\, d\lambda \right) d\mathbf{r} d\mathbf{r}'. \tag{2.22}$$

As the Coulomb interaction is spherically symmetric, only the spherical average of $h_{{\rm xc},\lambda}$ around $\mathbf{r}' = \mathbf{r}$ influences $E_{\rm xc}$. As a result, one can write [31]

$$E_{\rm xc} = N \int_0^\infty 2\pi\, u\, \bar{h}_{\rm xc}(u) du, \tag{2.23}$$

with $\mathbf{u} = \mathbf{r} - \mathbf{r}'$ and $\bar{h}_{\rm xc}(u)$ the system-, angle- and coupling-constant-averaged exchange-

correlation hole:

$$\bar{h}_{\mathrm{xc}}(u) = \frac{1}{N}\int_0^1 d\lambda \int \frac{d\Omega_{\mathbf{u}}}{4\pi} \int \rho(\mathbf{r})\, h_{\mathrm{xc},\lambda}(\mathbf{r}, \mathbf{r}+\mathbf{u}).d\mathbf{r} \tag{2.24}$$

Like the exchange-correlation energy, h_{xc} and $\bar{h}_{\mathrm{xc}}(u)$ can be decomposed into separate exchange and correlation holes. The exchange hole must be nonpositive everywhere and integrate to -1, whereas the correlation hole may change sign but must integrate to 0. Much of the successes (and failures) of approximate exchange-correlation functionals can be understood in terms of the properties of the exchange-correlation hole.

2.2.1 The local density approximation

The most basic (and arguably most important) approximation to the exchange-correlation energy is the local density approximation (LDA) [16], which starts out from the limit of a sufficiently slowly varying density. In this limit, it can be shown that the exact exchange-correlation functional is a local functional of the density:

$$E_{\mathrm{xc}}^{\mathrm{LDA}}[\rho_\downarrow, \rho_\uparrow] = \int \rho(\mathbf{r})\, \epsilon_{\mathrm{xc}}^{\mathrm{HEG}}(\rho_\downarrow, \rho_\uparrow)\, d\mathbf{r}, \tag{2.25}$$

with $\epsilon_{\mathrm{xc}}^{\mathrm{HEG}}(\rho_\downarrow, \rho_\uparrow)$ the exchange-correlation energy per electron in a homogeneous electron gas (HEG) with $\rho_\downarrow$ and $\rho_\uparrow$ spin densities. For the exchange part, the exact analytical solution is known [16, 32] and analytical expressions for the correlation energy density are obtained by parametrization of exact quantum Monte Carlo simulations of the HEG. Equations (2.28)-(2.29) show the parametrization by Perdew and Zunger [33] of the simulation results of Ceperley and Alder [34] for the unpolarized case ($\rho_\downarrow = \rho_\uparrow$).

$$\epsilon_{\mathrm{xc}}^{\mathrm{HEG}}(\rho) = \epsilon_{\mathrm{x}}^{\mathrm{HEG}}(\rho) + \epsilon_{\mathrm{c}}^{\mathrm{HEG}}(\rho), \tag{2.26}$$

$$\epsilon_{\mathrm{x}}^{\mathrm{HEG}}(r_s) = -\frac{3}{4\pi}\sqrt[3]{\frac{9\pi}{4}}\frac{1}{r_s}, \tag{2.27}$$

$$\epsilon_{\mathrm{c}}^{\mathrm{HEG}}(r_s) = -0.048 + 0.0311 \ln r_s + 0.0020\, r_s \ln r_s - 0.0116\, r_s \quad (r_s < 1), \tag{2.28}$$

$$= \frac{-0.1423}{1 + 1.0529\sqrt{r_s} + 0.3334\, r_s} \quad (r_s \geq 1). \tag{2.29}$$

The variable r_s corresponds to the radius of a sphere containing one electron:

$$r_s(\mathbf{r}) = \sqrt[3]{\frac{3}{4\pi\rho(\mathbf{r})}}. \tag{2.30}$$

The validity of the LDA expressions for the separate exchange and correlation energies is restricted to sufficiently slowly varying electron densities similar to the HEG (such as e.g. the valence electrons in simple bulk metals such as Al). The LDA exchange energy is also exact for the (non-relativistic) exchange energies of atoms in the limit of large atomic numbers [35]. The total $E_{\mathrm{xc}}^{\mathrm{LDA}}$ energy turns out to be also surprisingly well described in many other cases where large density gradients are present. For the G2-1 data set containing atomization energies of 55 small molecules, for example, the mean absolute error amounts to 1.6 eV [36]. Although this is a considerable error, it is circa four times smaller than for Hartree-Fock theory, and shows that the LDA can capture the essence of regular chemical bonding. The LDA systematically overbinds molecules with respect to atomization, and bond lengths are underestimated with mean absolute errors of circa 0.02 Å[37]. For solids the situation is similar, with consistent overestimation of cohesive energies and too short lattice constants [38].

The partial cancellation of errors in the separate exchange and correlation energies is not fortuitous, but stems from the fact that the local density approximation to the averaged exchange-correlation hole $\bar{h}_{\mathrm{xc}}$ is much more accurate than for the separate exchange and correlation holes. The separate holes are usually delocalized, whereas the LDA exchange and correlation hole are always centered around the position of the reference electron ($\mathbf{r} = \mathbf{r}'$). In many situations, however, the exact exchange and correlation holes cancel eachother fairly rapidly away from the reference position. It can furthermore be shown that the LDA on-top ($\mathbf{r} = \mathbf{r}'$) exchange-correlation hole depth is rather accurate [29, 31, 39] and that the LDA exchange and correlation holes satisfy the previously mentioned sum and sign rules. In addition, Equations (2.23-2.24) imply that the exchange-correlation energy is not very sensitive to details in h_{xc}. This also means that the difference between the spherical symmetry of the LDA exchange-correlation hole and the asymmetry of the exact hole is rather unimportant [40]. The moderate accuracy of the LDA total energy expression for typical inhomogeneous densities is therefore related to the fact that the relevant features of the corresponding exchange-correlation holes are similar to those in the HEG.

2.2.2 Generalized gradient approximations

Overall (and especially for atoms and molecules) a significant improvement is obtained when including the effect of the magnitude of the density gradient on the exchange-correlation energy. Generalized gradient approximations (GGAs) employ the gradient corrections to better describe the shape of the exchange-correlation hole close to the reference position (small values of u) [39], while making sure that the resulting functional

obeys the same exact constraints as the LDA. As the GGA form is more flexible than the LDA, GGAs can satisfy more exact constraints than the LDA. The Perdew-Wang (PW91) [30, 41] and Perdew-Burke-Ernzerhof (PBE) [42] functionals are the most well known amongst the non-empirical GGA functionals. Their general form can be written as:

$$E_{\mathrm{xc}}^{\mathrm{GGA}}[\rho_\downarrow, \rho_\uparrow] = E_{\mathrm{x}}^{\mathrm{GGA}}[\rho_\downarrow, \rho_\uparrow] + E_{\mathrm{c}}^{\mathrm{GGA}}[\rho_\downarrow, \rho_\uparrow], \tag{2.31}$$

$$E_{\mathrm{x}}^{\mathrm{GGA}}[\rho_\downarrow, \rho_\uparrow] = \int \rho(\mathbf{r})\, \epsilon_{\mathrm{x}}^{\mathrm{HEG}}(\rho_\downarrow, \rho_\uparrow)\, F_{\mathrm{x}}(\rho_\downarrow, \rho_\uparrow, |\nabla\rho|)\, d\mathbf{r}, \tag{2.32}$$

$$E_{\mathrm{c}}^{\mathrm{GGA}}[\rho_\downarrow, \rho_\uparrow] = \int \rho(\mathbf{r}) \left(\epsilon_{\mathrm{c}}^{\mathrm{HEG}}(\rho_\downarrow, \rho_\uparrow) + H_{\mathrm{c}}(\rho_\downarrow, \rho_\uparrow, |\nabla\rho|)\right) d\mathbf{r}. \tag{2.33}$$

The mean absolute error in the atomization energies of the G2-1 data is 0.37 eV with the PBE functional [36]. This constitutes a decrease by a factor of four compared to the LDA, at essentially the same computational cost. Also the barrier heights for gas-phase reactions are significantly improved as compared to the LDA: the mean absolute error in the BH76 set (containing 76 atom-transfer barrier heights) decreases from 0.64 eV (LDA) to 0.38 eV (PBE) [43]. The uniform improvement can be mainly attributed to a better *quantitative* description of the shape of the exchange-correlation hole nearest to the probe electron [39]. The GGA hole, however, retains the localized and spherically symmetric traits of the LDA hole.

For solids and clean surfaces, the comparison between GGAs and the LDA becomes more subtle. GGA functionals such as PBE and PW91 improve on the LDA results, though mainly in a statistical sense, not systematically [44, 45]. The LDA overestimation of cohesive energies, for example, is typically over-corrected [38]. Similarly, PBE lattice constants are on average 1-2% too long [38]. It has been argued that this behaviour is caused by the presence of diffuse tails of the exact hole [46]. Such features are less prominent in finite systems, and are not well captured by the PBE and PW91 functionals. It is, however, possible to construct alternative GGA functionals (such as WC [47] and AM05 [45]) which deliver improved accuracy in the solid state. Unfortunately, this type of improvement comes hand in hand with a worsened description of atoms and molecules [47–49].

2.2.3 Meta-generalized gradient approximations

Meta-GGA functionals, such as TPSS [50], M06-L [51] and SCAN [52], include second derivatives of the kinetic energy density into the exchange-correlation potential. While the description of finite systems is better compared to GGA functionals such as PBE, the improvement is again less uniform in the solid state [38]. Calculated lattice constants

are often more accurate, while cohesive energies remain difficult [38, 53]. However, the recently developed TM functional appears to be promising [54, 55].

2.2.4 Hybrid functionals

The largest errors of (meta-)GGA functionals in atomization energies involve molecules with multiple bonds. The binding energies of O_2, N_2, CO, and NO, for example, are all overestimated by the PW91 functional, with errors ranging between 0.4 and 1.0 eV [31, 56]. The difference in accuracy between single- and multiple-bonded molecules is related to differences in the exchange-correlation hole in the bonding region. In the case of multiple bonds, the exchange hole in between the nuclei becomes more delocalized due to the proximity of same-spin electrons [31]. The exchange-correlation hole is more localized than the exchange-only hole, but features remain which are not well captured by the localized GGA hole [57]. Consequently, the exchange-correlation energy (and therefore stability) of the molecule is overestimated compared to the atoms.

The error in the atomization energy arises mainly from the $\lambda = 0$ limit of the coupling-constant integration [56]. This means that improvements can be made by using the exact exchange energy at $\lambda = 0$ (see Equation 2.21) instead of the GGA exchange energy, while keeping the GGA expression for the exchange-correlation energy at $\lambda = 1$. This leads to the so-called 'hybrid' functionals [58], with the total exchange-correlation energy given by:

$$E_{\mathrm{xc}}^{\mathrm{hybr}} = \alpha\, E_{\mathrm{x}}^{\mathrm{HF}} + (1-\alpha)\, E_{\mathrm{x}}^{\mathrm{GGA}} + E_{\mathrm{c}}^{\mathrm{GGA}}. \tag{2.34}$$

The optimal amount α of Hartree-Fock (HF) exchange admixture depends on the curvature of the $E_{\mathrm{xc},\lambda}$ curve [59, 60]. For molecular atomization energies, α equal to $1/4$ has been shown to be most appropriate [59]. When applied to the PBE functional, the resulting 'PBE0' hybrid substantially improves the description of molecular geometries, thermochemistry and kinetics [36, 61]. The mean absolute errors in the G2-1 atomization energies and BH76 barrier heights, for example, are further reduced to 0.15 eV and 0.16 eV, respectively [36, 43].

Using the same amount of HF exchange also leads to improved descriptions of semiconductors and insulators, where the GGA underbinding is reduced [36, 62, 63]. Additionally, oxides such as CoO [64] and PdO [65] are correctly predicted to be semiconducting, whereas GGA functionals predict metallic behaviour. For most metals, however, including HF exchange enhances the underbinding by the parent GGA functional [62, 63, 66]. Due to (near-)degeneracy effects, the $E_{\mathrm{xc},\lambda}$ curve is such that it is preferable not to include HF exchange ($\alpha = 0$) [59]. In order to improve the GGA description for metals, it is the

$\lambda = 1$ end of the coupling-constant integration that needs to be addressed, rather than the shape of the $E_{\mathrm{xc},\lambda}$ curve.

An important drawback of 'global' hybrid functionals, such as PBE0, is that the non-locality of the exchange functional in Eq. (2.34) severely worsens the scaling of the computational cost with the number of electrons. For more efficient calculations on extended systems such as bulk materials or surfaces, it can be beneficial to neglect the minor contribution of the long-range part of the exact exchange interaction by screening the exchange potential. This results in 'screened' hybrid functionals, such as the Heyd-Scuseria-Ernzerhof (HSE) functionals [67–69]. In the HSE functionals, the exchange potential is screened using the complement of the error function:

$$E_{\mathrm{xc}}^{\mathrm{HSE}} = \alpha E_{\mathrm{x}}^{\mathrm{HF,SR}}(\omega) + (1-\alpha) E_{\mathrm{x}}^{\mathrm{PBE,SR}}(\omega) + E_{\mathrm{x}}^{\mathrm{PBE,LR}}(\omega) + E_{\mathrm{c}}^{\mathrm{PBE}}, \tag{2.35}$$

$$v_{\mathrm{x}}^{\mathrm{HF,SR}}(\mathbf{r},\mathbf{r}') = \frac{1-\mathrm{erf}(\omega|\mathbf{r}-\mathbf{r}'|)}{|\mathbf{r}-\mathbf{r}'|}. \tag{2.36}$$

The short- and long-range exchange potential is shown in Figure 2.1. The screening parameter ω has to be set small enough to retain agreement with the parent PBE0 functional, but as large as possible to improve the computational efficiency. Additionally, the accuracy in the G2-1 data set can actually be slightly enhanced over the PBE0 functional in a certain range of ω values. Based on these considerations, the optimal value for ω is chosen to be 0.11 Bohr^{-1} in the HSE06 functional (with $\alpha = 0.25$). There is, hence, a slight semi-empirical touch to the HSE functionals.

2.2.5 Limitations of semi-local and hybrid functionals

(Meta-)GGA and hybrid functionals have gained widespread use in materials science research, including the field of computational catalysis, thanks to a beneficial cost-to-accuracy ratio [70]. In this section, several shortcomings of these functional types are considered.

Fractional spins

The fractional spin constancy condition demands that the total energy remains constant when an electron is divided among degenerate frontier orbitals [71]. The energy of the hydrogen atom, for example, should be the same whether the electron density corresponds to that of the spin-up solution, the spin-down solution, or a convex combination of the two solutions (e.g. half spin up and half spin down). Another example is the oxygen atom, where all convex combinations of the $2s^2\,2p_x^{\mathbf{2}}\,2p_y^1\,2p_z^1$, $2s^2\,2p_x^1\,2p_y^{\mathbf{2}}\,2p_z^1$ and $2s^2\,2p_x^1\,2p_y^1\,2p_z^{\mathbf{2}}$

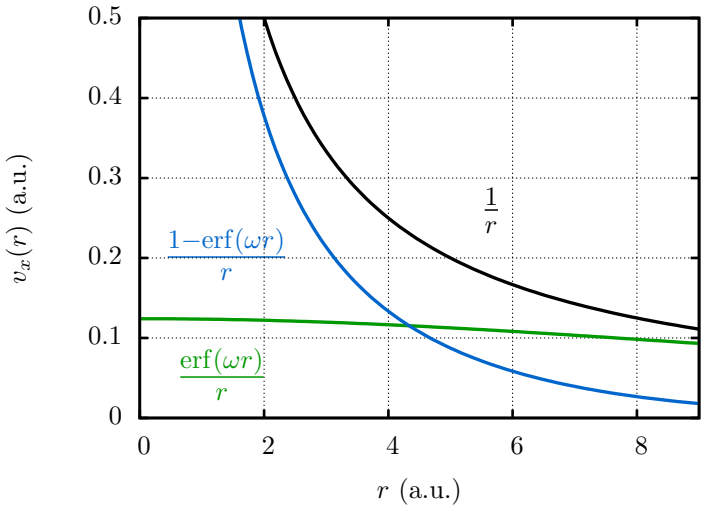

Figure 2.1: Plot of the Coulomb potential and its decomposition into long- and short-range parts using the error function for $\omega = 0.11$ Bohr^{-1}.

solutions ought to be degenerate. Almost all commonly used functionals, however, will attribute higher energies to the fractional combinations [72]. As a direct consequence, dissociation curves are not well described. When stretching the singlet H_2 molecule, for example, the separate H atoms adopt $1/2$ spin up and $1/2$ spin down densities, and the total energy is overestimated by several eV [73] As in the case of bulk metals, the curvature of the adiabatic connection curve is such that any amount of HF exchange will further worsen the GGA (or LDA) description [59]. This problem can also arise at equilibrium geometries, as in the example of O_3 [74]. A pragmatic solution is to (artificially) break the spin symmetry so that the integer-spin solution is retrieved [75, 76].

Fractional charges

The linearity condition for fractional charges states that the total energy must vary linearly between integer electron numbers [77]. Many density functionals, however, usually yield convex curves where fractional charge states are too low in energy. The stretched H_2^+ molecule serves as a minimal example [72], where the $H^+ \cdots H$ and $H^{0.5+} \cdots H^{0.5+}$ configurations are (near-)degenerate. Commonly used functionals, however, erroneously stabilize the configuration with fractional charges. This 'delocalization' error is largest (up to 2-3 eV) with LDA and GGA functionals, and reduces as the amount of HF exchange is increased [78]. This observation is easily explained in terms of the exchange-correlation hole, which for H_2^+ reduces to the exchange-only hole. In the case of $H^{0.5+} \cdots H^{0.5+}$, the

exact exchange hole is delocalized over both hydrogen atoms. The LDA and (meta-)GGA exchange-correlation hole is always localized around the position of the reference electron, and as a result the exchange-correlation energy is overestimated. The example of stretched H_2^+ is, however, a pathological case because correlation in many-electron compounds will partially localize the exchange-correlation hole. Reducing the delocalization error is known to be important for the description of barrier heights, and is often considered to be the main reason why hybrid functionals correct the underestimation of barrier heights by GGA functionals [79].

Other methods aim to reduce the delocalization error through orbital-dependent effective potentials. In the Perdew-Zunger self-interaction correction (PZ-SIC) approach [33], the total energy is corrected such that the (self-)Hartree and (self-)exchange-correlation energies cancel for every orbital. This scheme is accurate for single-electron systems and approximate otherwise [80]. Routine application of PZ-SIC is currently hampered by the need for unitary optimization of the orbitals and by the search for a compatible exchange-correlation functional [80, 81].

When the delocalization error involves a particular set of atomic orbitals, '+U' approaches can be applied where repulsive terms are added to destabilize fractional occupations [82–84]. Typical examples are d states in transition metal oxides and f states in rare-earth oxides.

Van der Waals interactions

Pure GGA and hybrid functionals do not account for van der Waals (vdW) forces, which are due to long-range electronic correlation between non-overlapping densities. Meta-GGA functionals are often able to capture vdW interactions at medium range [52]. One approach to describe the full range of vdW interactions is the Chalmers-Rutgers functional (vdW-DF [85]), which is based on the adiabatic connection. Methods employing the random phase approximation (RPA) can also be used [86, 87], albeit at much increased computational cost.

2.3 DFT in practice: the 'PWPAW' approach

As in the case of the functionals, there is a wide variety of approaches addressing the more 'technical' aspects of electronic structure calculations. One of these aspects is the basis set in which the wave functions are expanded. One straightforward option is to use a uniform real-space grid, as in the GPAW code [88, 89]. Another is to use a basis set of local functions centred around each atom, e.g. Gaussian-type functions. When applying

periodic boundary conditions, plane waves are a natural choice owing to their inherent periodicity. Another aspect is how to treat the different behaviour of core and valence electrons. Popular choices here are methods based on pseudopotentials and all-electron methods such as the projector augmented-wave (PAW) method. As the VASP code is a plane wave PAW code, it is these techniques that are given attention in the following paragraphs.

2.3.1 Kohn-Sham DFT with a plane wave basis

Bloch proved [90] that a one-electron Schrödinger equation with a periodic Hamiltonian has solutions which can be written as:

$$\psi_{\mathbf{k}}(\mathbf{r}) = u_{\mathbf{k}}(\mathbf{r}) \exp(i\mathbf{k} \cdot \mathbf{r}). \tag{2.37}$$

The $\mathbf{k}$-vectors reside in the reciprocal space spanned by the basis vectors $\mathbf{b}_i$:

$$\mathbf{k} = \sum_{i=1}^{3} k_i \mathbf{b}_i \ , \ \ k_i \in \mathbb{R}, \tag{2.38}$$

$$\mathbf{b}_1 = 2\pi \frac{\mathbf{a}_2 \times \mathbf{a}_3}{\mathbf{a}_1 \cdot (\mathbf{a}_2 \times \mathbf{a}_3)}, \tag{2.39}$$

where $\mathbf{a}_i$ are the real space lattice vectors ($\mathbf{b}_2$ and $\mathbf{b}_3$ follow by permutation). The function $u_{\mathbf{k}}(\mathbf{r})$ has the periodicity of the crystal, as has the potential energy operator (here in the form of the effective Kohn-Sham potential $v_{\text{eff}}(\mathbf{r})$), which means they can be represented using Fourier series. The relationships between $u_{\mathbf{k}}(\mathbf{r})$ and its Fourier coefficients $\hat{u}_{\mathbf{k}}(\mathbf{G})$ are:

$$u_{\mathbf{k}}(\mathbf{r}) = \sum_{\mathbf{G}} \hat{u}_{\mathbf{k}}(\mathbf{G}) \exp(i\mathbf{G} \cdot \mathbf{r}), \tag{2.40}$$

$$\hat{u}_{\mathbf{k}}(\mathbf{G}) = \frac{1}{V_{cell}} \int_{V_{cell}} u_{\mathbf{k}}(\mathbf{r}) \exp(-i\mathbf{G} \cdot \mathbf{r}) d\mathbf{r}. \tag{2.41}$$

The vectors of the reciprocal lattice are denoted by $\mathbf{G}$ ($= \sum_{i=1}^{3} G_i \mathbf{b}_i$, $G_i \in \mathbb{Z}$) and V_{cell} represents the volume of the unit cell.

The wave functions in general do not have the periodicity of the lattice, but are shifted in phase by a factor $\exp(i\mathbf{k} \cdot \mathbf{R})$ upon translation by a real space lattice vector

$\mathbf{R} = \sum_{i=1}^{3} N_i \mathbf{a}_i$, $N_i \in \mathbb{Z}$. For these we can write:

$$\psi_{\mathbf{k}}(\mathbf{r}) = \left(\sum_{\mathbf{G}} \hat{u}_{\mathbf{k}}(\mathbf{G}) \exp(i\mathbf{G} \cdot \mathbf{r}) \right) \exp(i\mathbf{k} \cdot \mathbf{r}), \tag{2.42}$$

$$= \sum_{\mathbf{G}} \hat{u}_{\mathbf{k}}(\mathbf{G}) \exp(i(\mathbf{k} + \mathbf{G}) \cdot \mathbf{r}). \tag{2.43}$$

If these expressions for $\psi_{\mathbf{k}}$ and v_{eff} are substituted in the real space Kohn-Sham equation,

$$\left(-\frac{1}{2}\nabla^2 + v_{\text{eff}}(\mathbf{r}) \right) \psi_{\mathbf{k}}(\mathbf{r}) = \epsilon_{\mathbf{k}} \psi_{\mathbf{k}}(\mathbf{r}), \tag{2.44}$$

the corresponding expression in reciprocal space becomes:

$$\frac{1}{2}|\mathbf{k} + \mathbf{G}|^2 \hat{u}_{\mathbf{k}}(\mathbf{G}) + \sum_{\mathbf{G}'} \hat{v}_{\text{eff}}(\mathbf{G} - \mathbf{G}') \hat{u}_{\mathbf{k}}(\mathbf{G}') = \epsilon_{\mathbf{k}} \hat{u}_{\mathbf{k}}(\mathbf{G}). \tag{2.45}$$

The eigenvalues and the Fourier coefficients $\hat{u}_{\mathbf{k}}(\mathbf{G})$ of the wave function are obtained by finding the eigenvalues and eigenvectors of the Hamiltonian matrix with elements:

$$H_{\mathbf{G},\mathbf{G}'}(\mathbf{k}) = \frac{1}{2}|\mathbf{k} + \mathbf{G}|^2 \delta_{\mathbf{G},\mathbf{G}'} + \hat{v}_{\text{eff}}(\mathbf{G} - \mathbf{G}'). \tag{2.46}$$

In practice, the number of reciprocal lattice vectors needs to be truncated, which is done by considering only those vectors corresponding to a kinetic energy smaller than a certain energy cut-off value ($\frac{1}{2}|\mathbf{k} + \mathbf{G}|^2 < E_{\text{cut}}$). This is appropriate as the magnitude of the terms in a Fourier series decreases rapidly as the norm of the frequency vector increases.

The problem now boils down to solving this eigenvalue problem for all $\mathbf{k} \in \mathbb{R}^3$. However, it follows from Bloch's theorem (Eq. (2.37)) that if $\psi_{\mathbf{k}}$ is a solution, then so is $\psi_{\mathbf{k}+\mathbf{G}}$. The solutions can therefore be restricted to $\mathbf{k}$-vectors inside a primitive unit cell of the reciprocal space (such as the first Brillouin zone). Now there are different solutions $\psi_{\mathbf{k},n}$ for such a $\mathbf{k}$, which are labeled by the band index $n = 0, 1, 2, ...$, with progressively higher eigenenergies $\epsilon_{\mathbf{k},n}$. In practice, the $\mathbf{k}$-dependence is handled through a discrete sampling of the (first) Brillouin zone. Additionally, only a finite number of bands needs to be considered, since there are only a finite number of electrons per unit cell.

The $\mathbf{k}$-point sampling in the calculations in this thesis is performed with the widely used method of Monkhorst and Pack [91, 92]. The method selects $\mathbf{k}$-points according to a

uniform ($N_1 \times N_2 \times N_3$) grid ($N_i$ **k**-points along the i^{th} reciprocal axis):

$$\mathbf{k}_{n_1,n_2,n_3} = \sum_{i=1}^{3} \frac{2n_i - N_i - 1}{2N_i} \mathbf{b}_i \quad , \quad n_i \in \{1 \dots N_i\}. \tag{2.47}$$

The mesh needs to be dense enough such that the Brillouin zone is sufficiently sampled to yield converged total energies. The set of **k**-points for which the Hamiltonian needs to be diagonalized is reduced by only considering the *irreducible* Brillouin zone, from which the contributions of the other **k**-points can be deduced by symmetry operations.

The different contributions to the Kohn-Sham potential $\hat{v}_{\text{eff}}(\mathbf{G})$ and the total electronic energy are obtained from the Hartree potential, the external potential arising from the nuclei, and the exchange-correlation potential. An expression for the Hartree energy (see Eq. (2.10)) can be derived starting from the Poisson equation in real space:

$$\nabla^2 v_{\text{Hartree}}(\mathbf{r}) = -4\pi\rho(\mathbf{r}). \tag{2.48}$$

After substitution of the Fourier expansions, this yields the corresponding expression in reciprocal space:

$$\hat{v}_{\text{Hartree}}(\mathbf{G}) = \frac{4\pi\hat{\rho}(\mathbf{G})}{|\mathbf{G}|^2}. \tag{2.49}$$

Using Plancherel's theorem [93], the Hartree energy per unit cell is given by:

$$E_{\text{Hartree}} = \frac{1}{2}\int_{V_{\text{cell}}} v_{\text{Hartree}}(\mathbf{r})\rho(\mathbf{r})d\mathbf{r} = 2\pi V_{\text{cell}} \sum_{\mathbf{G}\neq\mathbf{0}} \frac{\hat{\rho}(\mathbf{G})^2}{|\mathbf{G}|^2}. \tag{2.50}$$

The divergent term for $\mathbf{G} = \mathbf{0}$ has been omitted, as it cancels with the corresponding terms for the nucleus-nucleus and electron-nucleus interactions, provided the unit cell has no net charge.

The results for the external potential can be obtained in a similar way:

$$\nabla^2 v_{\text{ext}}(\mathbf{r}) = 4\pi \sum_m Z_m \, \delta(|\mathbf{r} - \mathbf{R}_m|), \tag{2.51}$$

$$\hat{v}_{\text{ext}}(\mathbf{G}) = -4\pi \sum_m Z_m \exp(-i\mathbf{G}\cdot\mathbf{R}_m)\frac{1}{|\mathbf{G}|^2}, \tag{2.52}$$

$$E_{\text{ext}} = -4\pi V_{\text{cell}} \sum_{\mathbf{G}\neq\mathbf{0}} \sum_m Z_m \exp(-i\mathbf{G}\cdot\mathbf{R}_m)\frac{\hat{\rho}(\mathbf{G})}{|\mathbf{G}|^2}. \tag{2.53}$$

The exchange-correlation potential, however, is typically determined in real space from the real space electron density $\rho(\mathbf{r})$. The Fourier coefficients $v_{\mathrm{xc}}(\mathbf{G})$ are then obtained by Fourier transformation.

2.3.2 The projector augmented-wave method

One important obstacle in performing efficient electronic structure calculations with plane wave basis sets is formed by the lowest energy electrons, which are located close to the atomic nucleus (the core electrons). Due to their strongly localized nature, they need to be represented with much finer resolution than the more extended valence electrons. Furthermore, the valence electron wave functions will show high frequency oscillations in the core regions, which are also numerically expensive to describe, especially in a plane wave basis set. Additionally, the valence electrons generally do not require explicit relativistic treatment, but the core electrons for heavier elements do.

Many different approaches have been formulated in order to solve this problem. One attractive approach is the projector augmented-wave (PAW) method developed by Blöchl [95]. It uses the idea from augmented plane wave (APW) methods to divide real space into spherical regions centred around the nuclei and the remaining interstitial region.

Inside these spheres, the wave functions are atomic-like and efficiently described using atomic-like basis functions (e.g. the solutions of the Kohn-Sham equation for the isolated atom) on logarithmic radial grids In the interstitial region, the wave functions vary smoothly, so that a plane wave basis (or a uniform real space grid) is more advantageous. In the PAW method, the wave functions ψ_j are described as smooth wave functions $\tilde{\psi}_j$ extending over the entire space to which corrections are added inside each 'augmentation sphere' m:

$$|\psi_j\rangle = |\tilde{\psi}_j\rangle + \sum_{m=1}^{M} (|\psi_j^m\rangle - |\tilde{\psi}_j^m\rangle). \tag{2.54}$$

As mentioned before, good choices for a 'partial waves' basis ϕ_i^m for ψ_j^m are the solutions of the (relativistic) Kohn-Sham equation for the isolated atom. Their expansion coefficients happen to be the same as for their smooth counterparts $\tilde{\psi}_j^m$ expanded in a basis of smooth partial waves $\tilde{\phi}_i^m$, which match the partial waves outside the augmentation spheres. These smooth partial waves can be chosen to be polynomials [89, 95] or Bessel functions [96]. It is in this way possible to construct a complete and orthonormal set of smooth projector functions $\tilde{p}_i^m$ that collect the expansion coefficients of the smooth part of the wave function

inside the augmentation sphere:

$$|\tilde{\psi}_j^m\rangle = \sum_i \langle \tilde{p}_i^m | \tilde{\psi}_i \rangle \, |\tilde{\phi}_i^m\rangle. \tag{2.55}$$

In this way the wave function can be written as:

$$|\psi_j\rangle = |\tilde{\psi}_j\rangle + \sum_{m=1}^{M} \left(\sum_i \langle \tilde{p}_i^m | \tilde{\psi}_i \rangle \, |\phi_i^m\rangle - \sum_i \langle \tilde{p}_i^m | \tilde{\psi}_i \rangle \, |\tilde{\phi}_i^m\rangle \right). \tag{2.56}$$

Similarly, the electron density can be viewed as a smooth density augmented by atomic corrections:

$$\rho(\mathbf{r}) = \tilde{\rho}(\mathbf{r}) + \sum_{m=1}^{M} (\rho^m(\mathbf{r}) - \tilde{\rho}^m(\mathbf{r})). \tag{2.57}$$

Finding the electronic ground state is in this scheme reduced to variationally optimizing the smooth part of the wave function only. For this quantity, the transformed Kohn-Sham Hamiltonian contains potential energy operators acting on the smooth density (evaluated using e.g. a plane wave basis set) plus corrections evaluated inside the augmentation spheres involving the partial waves and smooth partial waves (which can be evaluated efficiently using atom centered radial grids).

So far, the PAW method still provides an 'all-electron' description. In typical calculations, however, the frozen core approximation is invoked, which means the wave function for each frozen core state is considered constant and equal to its form of the reference atom. As sufficiently deep lying core states are typically quite inert in chemical processes, this is an efficient way of reducing the number of electrons that need to be explicitly taken into account. The atomization energies in the G2-1 data set, for example, have been shown to be affected by only a few meV/atom by this approximation [97]. Several additional approximations need to be made, such as truncating the (in principle infinite) number of (smooth) partial waves and projector functions, though also this can be done with very little loss in accuracy [95].

2.3.3 Finding the Kohn-Sham ground state

Generally the Kohn-Sham equations (2.12-2.18) need to be solved iteratively. In plane wave codes, the superposition of the atomic charge densities is typically used as an initial

guess for the total density. As the density determines the Kohn-Sham Hamiltonian matrix $H_{\mathbf{G},\mathbf{G}'}(\mathbf{k})$ (Eq. 2.46), the initial wave functions could in principle be obtained after full diagonalization at every $\mathbf{k}$-point. Using the lowest occupied states a new charge density can then be constructed. This is iterated until the convergence thresholds are met (e.g. less than 10^{-5} eV changes in the energy).

Due to the large size of the plane wave basis set, however, full diagonalization as well as storage of the Hamiltonian must be avoided. Most plane wave codes, including VASP, employ algorithms where only diagonalization in the subspace of the occupied orbitals is needed. In such schemes, the initial wave functions are randomly generated, and the electron density and wave functions are alternatingly updated until self-consistency is reached [98].

Chapter 3

From electronic energies to measurable properties

This chapter deals with methods used in this thesis to link the first-principles description of the electronic structure to experimentally measurable quantities. The different connections are illustrated in Figure 3.1, which depicts a metal nanoparticle with O and CO adsorbates. Firstly, the binding energies of the core electrons in the different atoms can be measured by X-ray photoemission. Also infrared radiation may used to probe the properties of the adsorbates by exciting certain molecular vibrations such as the C-O stretch. Lastly, the rate of product formation can be quantified via e.g. mass spectrometry. There are of course many other available techniques in heterogeneous catalysis research to probe reactions and the state of the catalyst (see e.g. Ref. [99]).

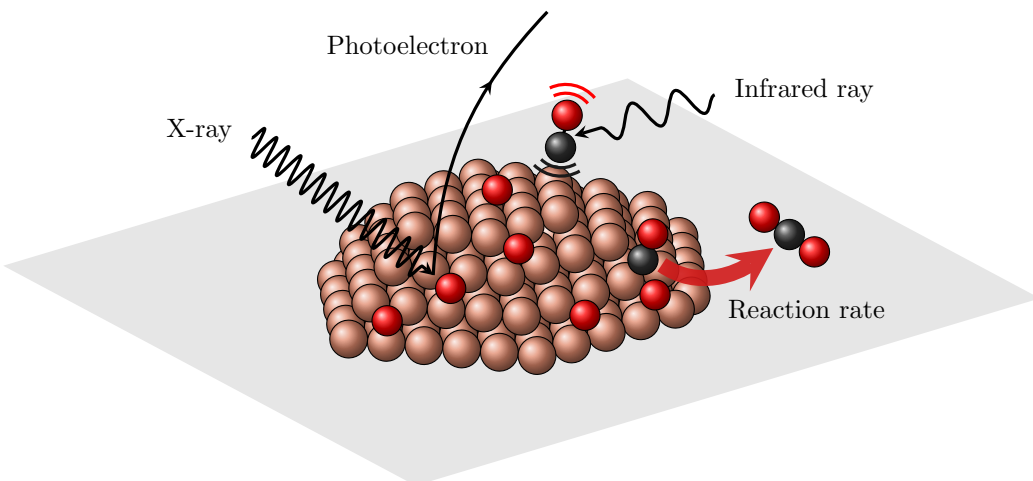

Figure 3.1: Cartoon representation [100] of a metal nanoparticle with O and CO adsorbates and illustration of different experimental measurement principles.

3.1 Core-level spectroscopy

Core-level spectroscopy is a powerful technique to investigate the structure and chemical environment of the atoms close to the sample surface [101]. It uses X-ray photons to measure the binding energies of core electrons (e.g. the $3d_{5/2}$ level in Pd atoms), based on the photoelectric effect. Synchrotrons are often the preferred X-ray radiation sources, thanks to the high energy resolution and tunability of the X-ray beams [102].

Comparisons between the measured photoemission spectrum and theoretical predictions for different structures has proven to be a fruitful approach for elucidating surface structures and adsorbate geometries [103–106]. Direct reproduction of the experimental binding energy spectrum is, however, rarely attempted, for two reasons. One is that absolute binding energies of core electrons with respect to e.g. the Fermi level are difficult to calculate with high accuracy. Secondly, also the precise line shape is difficult to reproduce, requiring e.g. time dependent DFT or many-body perturbation techniques [107] such as the GW approach [108]. However, for interpreting core-level spectra without significant shake-up or shake-down satellites, it is sufficient to only calculate the relative shifts between the centers of the main peaks in the spectrum. Such relative peak shifts are easier to calculate with reliable accuracy [109] and are referred to as the core-level shifts (CLS).

3.1.1 The complete screening picture

In the complete screening picture, the CLS is calculated as the energy difference:

$$\mathrm{CLS} = [E_* - E_0] - [E_*^{\mathrm{ref}} - E_0^{\mathrm{ref}}], \tag{3.1}$$

with E_0 and E_* representing (valence) ground state energies of the unperturbed material and in presence of a core-hole in one of the atoms, respectively. This total energy approach relies on four main approximations regarding the final state, i.e. the electronic state of the material when the photoelectron has left the system:

(1.) The core-hole has not yet decayed, i.e. its lifetime is long compared to the photoemission process itself. This is indeed true in the case of not too heavy atoms and not too deep levels [110–112], where intra-atomic Auger decay of the core-hole is sufficiently slow [113].

(2.) The valence electrons are considered to be in the ground state (with the constraint of a core-hole). Including the relaxation of the valence electrons is often crucial for accurately determining the CLS [114–117].

(3.) The remaining core electrons can be treated in different of ways: (i) by using pseudopotentials that have been generated for an ionized reference atom, (ii) by simply substituting the atom with the next element in the periodic table, the so-called 'Z+1' or 'equivalent core' approximation [118], and (iii) by removing the core state (in all-electron methods) and either relaxing the other core electrons (while maintaining orthogonality towards the core-hole) or keeping the remaining core electrons frozen (as done in the PAW implementation in VASP). These different methods yield similar results, although the 'Z+1' approximation only holds for sufficiently deep core-holes [119]. The reason for this similarity is that the relaxation of the core electrons is rather unimportant for the CLS, because this relaxation is quite independent of the chemical environment [120, 121].

(4.) The effect of structural relaxation is neglected. Except for light atoms in molecules or light molecular adsorbates, these vibrational excitations in the final state do not contribute significantly to the measured binding energy thanks to the slow response of the nuclei in comparison to the electrons [112].

The use of periodic boundary conditions prohibits the use of charged supercells, as charge neutrality needs to be maintained. This can be done either by adding an extra electron to the valence or by adding the compensating charge as a homogeneous 'jellium' background. Adding an electron to the valence band is the better approach if there is a high density of states at the Fermi level, but is problematic for insulators and semiconductors, in which case the jellium background approach is preferred. In the jellium approach, the total electronic energy does not converge with respect to the vacuum distance between periodically repeated images. This would call for the application of charged supercell corrections of the total energy [122] but such corrections largely cancel out when the CLS is calculated between two atoms in the same unit cell. In that case the CLS expression reduces to:

$$\mathrm{CLS} = E_* - E_*^{\mathrm{ref}}, \tag{3.2}$$

which has the additional benefit of accelerating the convergence with respect to k-point sampling, energy cutoff, inter-slab distance and slab dimensions [121].

3.1.2 Initial and final state contributions

In order to understand the origin of the CLS, it can be useful to decompose the CLS in so-called initial and final state shifts. The initial state contribution is related to differences

in the charge density in the initial ground state, whereas the final state contribution arises because of differences in the screening of the core-hole in the final state [101, 123]. While such a decomposition is to an extent arbitrary and only the total shift can be measured experimentally [124], it can be used to understand the origin of these shifts. Within Kohn-Sham DFT it is reasonable to associate the initial state shift with the negative of the shift in the core electron eigenvalue [125, 126]. The eigenvalue shift is furthermore closely related to the difference in electrostatic potential at the nuclei [101, 123, 124, 127]. Trends in core-level shifts can in some cases be understood in terms of the initial state shifts alone, as for the surface CLS across different transition metal surfaces [128]. In other situations, such as e.g. surface alloys [129] or adsorbate-covered substrates [117, 130, 131], trends across different elements are complicated by variations in the final state contribution to the total CLS.

3.2 Geometry optimization

The most relevant molecular structures for many properties (such as the spectroscopic properties described in the previous section) are the 'equilibrium geometries' where the molecule adopts a local or global energy minimum with respect to displacement of the nuclei. Another type of configuration of particular interest in reaction rate theory are the 'transition states' corresponding to the minimum energy barrier separating reactants and products. Methods to find these three types of structures are sketched in the next sections.

3.2.1 Finding a local minimum

Finding the closest local minimum to a certain initial geometry guess is a matter of applying a suitable algorithm to minimize the total energy with respect to the positions of the nuclei. All efficient minimization methods require knowledge of the forces f_i along each nuclear coordinate i:

$$f_i = -\frac{\partial E}{\partial R_i}. \tag{3.3}$$

From the Hellmann-Feynman theorem it can be shown that this force only depends on the charge density and the change in the Coulomb potential of the nuclei, i.e. just classical electrostatic forces [132]:

$$f_i = -\int \rho(\boldsymbol{r}) \frac{\partial V_{\text{ext}}(\boldsymbol{r}, \boldsymbol{R})}{\partial R_i} d\boldsymbol{r} - \frac{\partial E_{i-i}}{\partial R_i}. \tag{3.4}$$

The iterative process of computing the forces and generating successive structures is pursued until the chosen convergence criteria are met. For most purposes, a suitable criterion is that the norm of the force on each atom is below 10^{-2} eV/Å . In this thesis mostly the conjugate gradient, BFGS [133] and FIRE [134] algorithms have been used.

3.2.2 Finding the global minimum

In many cases one is interested in finding not just a local (free) energy minimum but rather the most stable local minimum – the global minimum (GM). Common examples include finding the most stable configurations of nanoparticles, molecular adsorbates, surface structures and bulk crystal structures. In case there are few local minima, the GM can be found 'manually' through an exhaustive search or educated guess. However, as the degrees of freedom increase automated search heuristics become necessary. Many global minimization methods have thus far been developed, including simulated annealing [135, 136], genetic algorithms (GAs) [137], basin hopping [138], minima hopping [139], and particle-swarm optimization [140]. The literature is sparse on comparisons between different global minimization methods for chemical structures, and it has been argued that the optimal algorithm is likely to be system dependent [141]. GAs are however generally considered to be advantageous for complex potential energy landscapes [142] and have seen diverse application, ranging from clusters [143] to bulk crystals [144].

In this thesis, the genetic algorithm (GA) module [145] from the ASE package [146] has been used. The general outline of a genetic algorithm run is shown in Figure 3.2. First, an initial database is created from randomly generated structures subjected to local minimization. From the database a 'population' is drawn containing the most stable unique structures. Typical population counts range from 10 to 30. New structures are then created from the population, locally minimized, and added to the database.

In order to spawn new structures from existing ones, one or several genetic operators need to be defined. 'Pairing' operators, for example, combine random parts from two parent structures into a new structure. 'Mutations' operate only on one structure, by e.g. subjecting the atoms to random displacements. Inside the main loop, operators are picked at random according to user-defined weights. Selecting structures from the population also happens randomly, with a weight distribution favouring the more stable structures.

As the GA run proceeds, the population will contain increasingly stable structures, and will hopefully include the GM before the iteration limit is reached. Because GAs are stochastic procedures, the number of required iterations to find the GM varies from run to run. Consequently, several GA runs are typically executed in parallel. It is often the initial structure generation and the choice of genetic operators that have the largest impact on

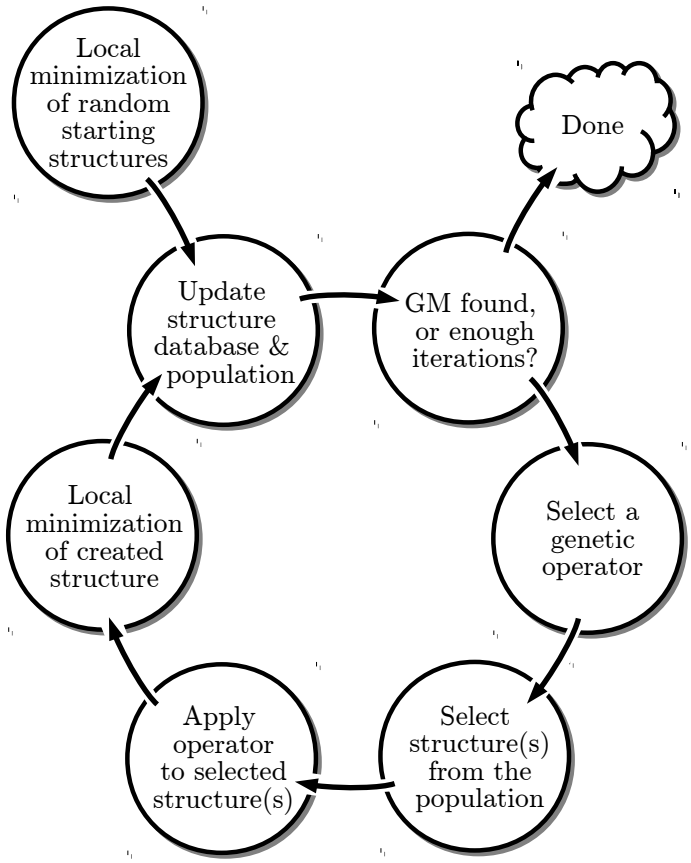

Figure 3.2: Flow chart of a genetic algorithm run.

the efficiency of the GA [147, 148]. Many applications therefore feature custom-designed operators that are expected to increase the performance for the problem at hand.

3.2.3 Finding a transition state

The transition state for a chemical reaction is defined as the lowest energy saddle point connecting the reactants and the reaction products (more on that in Section 3.4). Saddle points are local minima on the potential energy surface in all directions except for the mode along which the reaction occurs, where the saddle point is a local maximum. In principle, the second derivatives of the potential energy would be helpful in finding such transition states, since they describe the local curvature of the potential energy landscape.

In plane wave DFT codes, however, these second derivatives are not readily computed (see Section 3.3), so different methods have been developed which rely only on first derivatives.

The nudged elastic band method

In the nudged elastic band (NEB) method [150–152], as the name suggests, the idea is to span an elastic band between the reactant state and the product state and to optimize this band so that it follows the minimum energy pathway between them. The procedure is started by constructing a band of intermediates and specifying the spring constant of the spring forces between successive intermediates in the band, so as to keep them equidistant. If the forces on the nuclei for each image are calculated, then following the components of the forces perpendicular to the band will lead to convergence towards the minimum energy pathway. A convenient variant is the climbing image NEB method, where, in addition, the energy of the highest intermediate is maximized and hence converges to the energy of the transition state.

The dimer method

The NEB method requires knowledge of the product state and involves ground state calculations for a large number of intermediates in order to resolve the minimum energy pathway. While it constitutes a rather robust method, it can be excessive if only information about the transition state is required. The dimer method [153] involves only two structures (the 'dimer'), both slightly displaced from the center of the dimer along a particular direction. Through a series of translations and rotations of the dimer, the center of the dimer is moved to the nearest saddle point for the given initial direction. From the forces on the dimer structures, it is possible to estimate the rotation angle necessary to align the dimer along the direction with lowest curvature. One can translate the dimer following a modified force which points towards the saddle point.

3.3 Vibrational frequencies

Molecules vibrate at characteristic frequencies, related to the molecular bond acting as a spring that counteracts a displacement of the atoms from their equilibrium positions. Estimating the vibrational frequencies can be useful for interpreting infrared spectroscopy measurements and for evaluating the vibrational entropy and energy contributions to thermodynamic properties.

This is often done in the harmonic approximation. In this approximation, the displacements are assumed to be sufficiently small, so that the potential energy scales quadratically.

The modes in which the atoms vibrate and their energy levels can then be obtained by diagonalizing the mass-weighted Hessian matrix. Each mode i has the following allowed energy levels:

$$E_{i,n} = \hbar\omega_i \left(\frac{1}{2} + n\right) \quad , \quad n = 0, 1, 2, \ldots . \tag{3.5}$$

If the molecule is isolated, six of these modes will have (near-)zero frequencies ω_i, corresponding to translation and rotation of the whole molecule (five in the case of a linear molecule). The remaining modes are associated with true vibrations, such as the stretching of the C-O bond in the CO molecule. In the case of modes with a negative energy curvature, as along the reaction coordinate at a saddle point, ω_i will be imaginary.

3.4 Rates of reactions on surfaces

Estimating the rates of elementary reactions from first principles is important to construct theoretical models that describe the preferred reaction mechanism for a chemical process. Also the catalytic activity of materials that are not yet experimentally synthesized can be evaluated in this way. One could, in principle, perform ab initio molecular dynamics simulations, explicitly propagating a collection of molecules on a surface, from which reaction rates can be extracted. This, however, is presently not an option, mainly because of the extremely wide separation of time scales for molecular vibrations ($\sim 10^{13}$ Hz) and activated chemical reactions (down to 1 Hz or less). This viewpoint, however, opens up possibilities for useful approximate theories [154, 155].

3.4.1 Transition state theory

A solution to the time scale separation problem is to coarse-grain the phase space that is sampled in the molecular dynamics simulations. Instead of resolving all the atomic positions and momenta, the time evolution can be modelled as the hopping between different local minima of the free energy landscape. In the context of surface reactions, such a local minimum is associated with a specific spatial arrangement of adsorbates on the surface. Each such 'configuration' describes which adsorbates are bound to which adsorption sites. Neighbouring configurations are hence separated by a single diffusive or reactive event. After assuming thermal equilibration within the basin of the local minimum, the probability $P_\alpha(t)$ of observing the specific configuration α at a certain time

t obeys a gain-loss type equation called the Master Equation:

$$\frac{\partial P_\alpha(t)}{\partial t} = \sum_\beta W_{\beta\to\alpha} P_\beta(t) - \sum_\beta W_{\alpha\to\beta} P_\alpha(t). \tag{3.6}$$

The 'transition frequency' $W_{\alpha\to\beta}$ denotes the frequency at which a configuration α transforms into a neighbouring configuration β. It can be shown that expressions for these transition frequencies are given by the ones familiar from conventional transition state theory (TST)[1] developed by Eyring [158], Evans and Polanyi [159]:

$$W_{\alpha\to\beta} = \frac{k_\mathrm{B}T}{h}\frac{Q_\ddagger}{Q_\alpha} = \frac{k_\mathrm{B}T}{h}\frac{q_\ddagger}{q_\mathrm{reactants}}, \tag{3.7}$$

$$W_{\beta\to\alpha} = \frac{k_\mathrm{B}T}{h}\frac{Q_\ddagger}{Q_\beta} = \frac{k_\mathrm{B}T}{h}\frac{q_\ddagger}{q_\mathrm{products}}. \tag{3.8}$$

The label ‡ refers to the 'transition state', which corresponds to a saddle point on the energy landscape representing the minimum energy barrier separating α and β configurations. For the right hand side equalities in Eq. (3.7-3.8) it has been assumed that the total partition function Q can be written as the product of the single-adsorbate partition functions q. As a result, only the partition functions of the adsorbates directly participating in the reaction enter the expression for the transition frequency W.

The partition functions q are typically evaluated[2] using simple statistical mechanical models (such as the quantum harmonic oscillator, rigid rotor, particle in a box) after assuming separability of e.g. translational, rotational, vibrational and electronic contributions to the total partition function (for further information, see e.g. Ref. [99]). The link to the well known Arrhenius equation [160] is easier to recognize if in Eq. (3.7) the electronic partition functions are evaluated with respect to their own potential energy minimum:

$$W_{\alpha\to\beta} = \frac{k_\mathrm{B}T}{h}\frac{q'_\ddagger}{q'_\alpha}\exp\left(-\frac{E_{el,\ddagger} - E_{el,\alpha}}{k_\mathrm{B}T}\right). \tag{3.9}$$

3.4.2 Mean-field kinetic modelling

The evolution of the adsorbate configurations on the surface, i.e. the probabilities $P_\alpha(t)$, can in principle be obtained by integrating the Master Equation (3.6), starting from

[1] For conventional TST the additional 'no-recrossing' approximation needs to be made [156], meaning that every trajectory crossing the phase space boundary between α and β actually results in the transformation to β. This is in general a very suitable approximation [157].

[2] This is commonly done in a canonical ensemble so as to yield 'Boltzmann' transition frequencies, which have been averaged over the internal states of the reactants.

a chosen initial configuration. As the number of possible configurations α is typically extremely large,[3] direct numerical integration is infeasible. Kinetic Monte Carlo methods carry out the integration more efficiently through the use of stochastic techniques [161]. Since these methods come with a significant computational cost, usually simpler and more efficient (though potentially less accurate) procedures are employed.

In the mean-field approximation, the adsorbates are assumed to be uniformly distributed over the surface, so that the probability of finding an adsorbate i on a lattice site is the same and equal to its fractional coverage θ_i. This is only strictly justified if (i) the surface is uniform, (ii) the number of sites is sufficiently large, (iii) the diffusion of the adsorbates over the surface is sufficiently fast and (iv) lateral interactions (repulsive of attractive forces between adsorbates) are weak [154, 162, 163]. This approximation allows to derive the typical mean-field rate equations from the Master Equation [154]. In the case of a bimolecular reaction between i and j adsorbates, the expression of the reaction rate is given by:[4]

$$r = W\theta_{(i,j)-\text{pairs}} \xrightarrow[approximation]{mean-field} r = WZ\theta_i\theta_j. \tag{3.10}$$

Z is the coordination number of the lattice, i.e. the number of nearest-neighbour sites around a site. The coverage dependence of the transition frequency W can be included in an approximate manner by using the mean-field probabilities for the different possible occupations of the sites that surround the reactant(s).

With a set of adsorbates and elementary reactions, the time evolution of the coverages $\boldsymbol{\theta}$ can be simulated together with the reaction rates $\boldsymbol{r}$ by integrating the following set of coupled differential equations:

$$\frac{\partial\theta_i(t)}{\partial t} = \sum_{\text{reaction } k} c_{ik} r_k(\boldsymbol{\theta}(t)). \tag{3.11}$$

where c_{ik} is the number of adsorbates i consumed ($c_{ik} < 0$) or produced ($c_{ik} > 0$) in a reaction k. In this thesis the open source `SciPy` Python package is used for performing such numerical integrations, which wraps around the widely used `odepack` Fortran library [164].

[3] For a surface with M sites and N adsorbates, the total number of configurations equals $(N+1)^M$.
[4] This shows that the transition frequencies W and macroscopic rate coefficients k relate as $k = Z\,W$.

3.4.3 Quasi-chemical kinetic modelling

The mean-field rate equations become increasingly inaccurate as the lateral interaction strengths exceed the thermal energy $k_{\mathrm{B}}T$ [162, 165]. In such cases the quasi-chemical approximation presents an alternative approach, without having to resort to Monte Carlo simulations. Instead of describing the surface coverage in terms of single-site probabilities θ_i, the two-site probabilities τ_{ij} are introduced which describe the probability that two neighbouring sites are occupied by a pair of i and j adsorbates. Given the global coverages θ_i, the distribution of each adsorbate i among the different (i, j) pairs can be calculated from equilibrium thermodynamics (assuming fast surface diffusion).

The main approximation in terms of lateral interactions lies in the evaluation of the energetical preference of the different (i, j) pairs. There, the probability that a site next to the i (resp. j) adsorbate is occupied by k is assumed to be equal to τ_{ik} (resp. τ_{jk}). This means that the correlations between the different neighbours around the site pair are neglected.

The probabilities τ_{ij} cannot usually be expressed in closed form and hence need to be computed iteratively [162]. The coverage derivatives can then be calculated as in Equation (3.11) by using the pair probabilities τ_{ij} in the evaluation of the reaction rates. As in the case of the mean-field approximation, the coverage dependence of the transition frequencies can be included if desired.

This scheme is in general approximate, but becomes exact if the surface lattice only has one-dimensional periodicity [162, 165]. The PdO(101) surface is such a case, because the parallel rows of reactive threefold coordinated O and Pd atoms are separated by rows of relatively inert fourfold coordinated O and Pd atoms (see Chapter 5). Edge sites on stepped Ru surfaces are another example [166, 167].

Chapter 4

Reactions on surfaces

4.1 Catalytic processes

The term 'catalysis' was coined in the early 19$^{\text{th}}$ century by the Swedish scientist Berzelius, to refer to phenomena where a small amount of a foreign substance has a great influence on the course of a chemical reaction [168]. Early examples were Döbereiner's experiments with ignition of a hydrogen-air stream using platinum powder [169]. The word derives from the ancient Greek verb καταλύειν meaning 'breaking down', implying that the catalyst decomposes the reactants and so facilitates the formation of the reaction products. Ostwald [170] later offered a more precise definition of a catalyst: a substance that changes the rate of a chemical reaction without being consumed.

Catalysts can be classified as homogeneous, heterogeneous and enzymatic [171]. Homogeneous catalysts are part of the same fluid phase as the reactants, whereas heterogeneous catalysts (usually a solid surface) form a phase separate from that of the reactants. Enzymatic catalysts are a special case of homogeneous catalysis, referring to large, complex biomolecules. Of these three types, the heterogeneous catalysts have the distinct advantage of being easy to separate from the reactant phase, which has led to innumerable industrial applications [172]. Homogeneous and enzymatic catalysts, however, often allow better control of product selectivity [173].

The first step in the heterogeneous catalytic process, as sketched in Figure 4.1, is the binding of the reactants from the fluid phase to the catalyst surface. Once they are adsorbed, molecules often undergo dissociation steps where they are separated into smaller fragments (e.g. O_2 dissociating into O atoms). After adsorption, the species can diffuse over the surface. When two reactants are in close proximity, reaction products can be formed. The catalytic cycle is completed by the desorption of these products into the fluid phase, with the surface sites becoming available again for reaction.

The reaction mechanism depicted in Figure 4.1 is of Langmuir-Hinshelwood type, where the products are formed by reactions between adsorbed species [174]. Another possibility is that gas phase molecules react directly with adsorbates, which is referred to as an Eley-Rideal mechanism [175]. Yet another type is the Mars-van Krevelen mechanism,

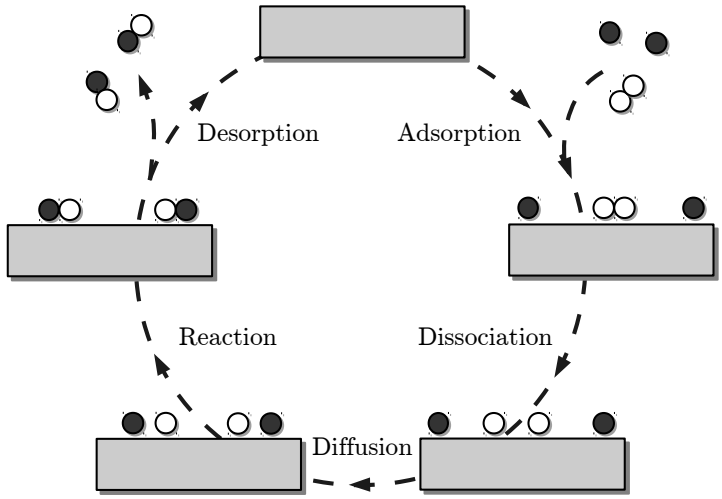

Figure 4.1: Diagram of a simple catalytic cycle for the reaction $A_2 + 2\ B \rightarrow 2\ AB$.

where atoms of the substrate lattice act as reactants and become part of the product molecule [176]. This can for example occur on surfaces of reducible oxides such as the PdO(101) surface.

One of many considerations when using catalysts to speed up a chemical process, is the activity of the catalyst. Catalytic activity is commonly defined as the net rate at which the reactants are converted into products. The rate is usually normalized, e.g. per unit weight of the catalyst, per mole of the precious metal, or per surface atom of the active component. In this definition, the catalytic activity of a material is in general a time dependent property, as well as a function of the local reaction conditions (temperature and partial pressures).

In many applications, such as the total oxidation of methane, the performance of the catalytic reactor is limited by the activity of the catalyst. Although the total activity may be the result from numerous reaction pathways and may involve many different surface species, it is to a first order approximation only sensitive to the stability of a small subset of intermediates and transition states [177]. One particular reaction step may for example be kinetically relevant due to a high free energy of activation. This is often the case for the first C-H dissocation step in methane oxidation catalysis [178]. Another example is the CO oxidation activity of several transition metal catalysts, which is sensitive to the stability of adsorbed CO under typical low-temperature conditions [179]. Understanding the origins of a catalyst's limited activity in terms of its structural and electronic properties can then be reduced to understanding how these relevant intermediates and activated complexes are bound to the catalyst surface.

4.2 Bonding on surfaces

Even though accurate electronic structure methods allow for detailed descriptions of the interaction between molecules and a catalyst surface, it is often more insightful to analyze the bonding in simpler, more qualitative terms. In frontier molecular orbital theory [180–182] the interaction between two fragments (such as the adsorbate and the surface) is described in terms of the energies and shapes of the 'frontier' molecular orbitals (MOs). These usually consist of the highest occupied and lowest unoccupied MOs (HOMO and LUMO) of each fragment.

In the following paragraphs, the bonding in different surface-adsorbate combinations will be discussed to provide a background for the discussion in Chapter 5. First the adsorption of CO on a transition metal surface will be discussed, followed by adsorption of CO and H on the surface of a transition metal oxide.

4.2.1 Bonding to a transition metal surface

Blyholder was among the first to apply a MO analysis to bonding of CO to d-metal surfaces [183]. Here, the most important frontier MOs in CO are the 5σ (HOMO)and $2\pi^*$ (LUMO) states. The 5σ MO can be regarded as a lone electron pair situated at the carbon end of the molecule, whereas the $2\pi^*$ MO has lobes on both the carbon and oxygen atoms (see Figure 4.2). The most relevant frontier MOs of the substrate are the metal d states, in particular those with d_{z^2}, d_{xz} and d_{yz} character.

The transition metal surface offers several sites for CO adsorption (see Figure 4.2). In the 'atop' position, a linear M-CO bond is formed. The main bonding contributions originate from the interaction between the CO 5σ and metal d_{z^2} states, which yields

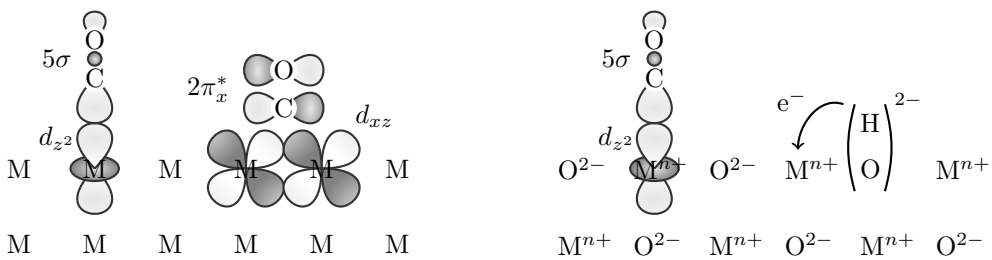

Figure 4.2: Schematics for adsorbate binding to different surfaces. Left: CO in atop and bridge position of a transition metal surface. Right: CO and H adsorption on the surface of a transition metal monoxide. Changes in the sign of the orbital lobes are indicated by difference in shading.

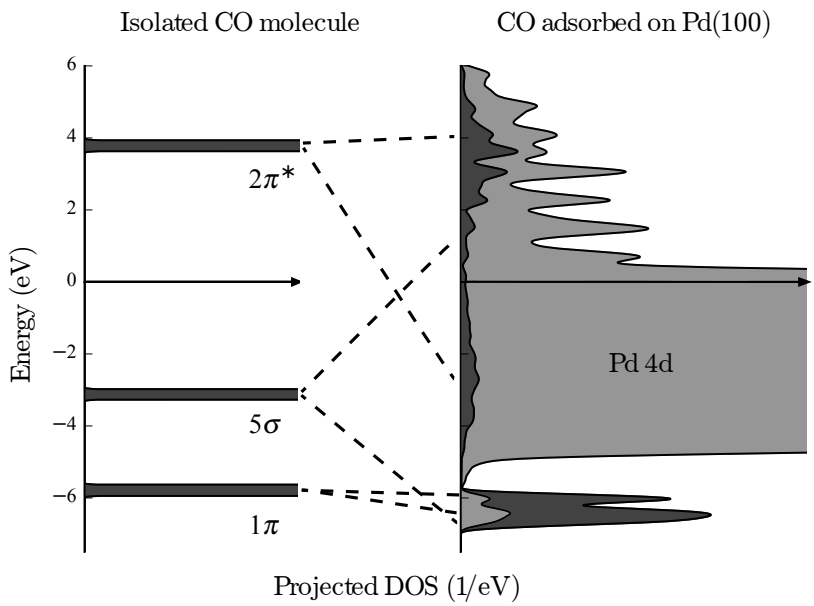

Figure 4.3: Density of states calculated with the PBE functional for bridge-adsorbed CO on Pd(100). Left: the density of states in the isolated CO molecule. Right: the density of states projected on the CO s, p and Pd $4d$ states when CO is adsorbed in a bridge position on a Pd(100) surface slab.

bonding and anti-bonding combinations (see Figure 4.3). As the anti-bonding combinations lie partly above the Fermi level, this has a net bonding effect. In this process the population of the 5σ MO is reduced – this is called 'σ-donation'.

In the 'bridge' position, the CO molecule is located in between two transition metal atoms. Compared to the atop site, there is now an increased overlap between the unoccupied CO $2\pi^*$ and the (partially) occupied metal d_{xz} and d_{yz} states. Due to their higher energies with respect to the Fermi level, almost exclusively the bonding combinations get occupied, which contribute to the Pd-CO bond. This is called 'π-backdonation', as the population of the $2\pi^*$ MO is now increased. As this MO is anti-bonding with respect to the C-O bond, this bond is weakened, leading to a larger C-O distance and a lower vibrational frequency [183].

This picture is captured in the d-band model of Hammer and Nørskov [185, 186], which is often used to explain variations between the adsorption properties of different d-metals.[1]

[1]The d-band description is based on the Newns-Anderson model [187, 188], which can be seen as a band-theoretical approach to chemisorption.

The CO and O adsorption energies, for example, are dependent on the position of the d-band center: if the d-band is more than half filled, then moving the d-band center closer to the Fermi level will increase the interaction with unoccupied states of the molecule such as the CO $2\pi^*$ MO, which increases the adsorption energy.

It should be noted that the above picture is approximate, as experimental measurements have shown that also the 1π MO is involved in the bonding [189, 190]. This is supported by electronic structure calculations which indicate that the 1π and $2\pi^*$ rehybridize upon adsorption [189, 191]. Figure 4.3 also indicates that the 1π state is affected upon CO adsorption.

4.2.2 Bonding to a transition metal oxide surface

Owing to the transfer of charge from the metal to oxygen atoms, the electronic structure of transition metal atoms differs in several ways from the metal. The most notable differences are:

- A reduced d-electron count.
- A widening of the metal d-band due to overlap with the O $2p$ states.
- The presence of a band gap.

Considering CO binding to the metal atoms at the surface, σ-donation and π-backdonation processes may occur as on the transition metal surface. For significant 5σ-donation, the metal d_{z^2} states need to be sufficiently depopulated, while for $2\pi^*$-backdonation occupied d_{xz} and d_{yz} states are needed. For CO adsorption on top of an undercoordinated Pd atom of the PdO(101) surface, the main contribution to the bonding arises from σ-donation (see Figure 4.4). Due to the slightly anti-bonding character of the 5σ MO with respect to the C-O bond [192], the C-O stretching frequency can actually increase compared to the gas phase [193].

Transition metal oxide surfaces also feature undercoordinated O atoms on which molecules may adsorb. Atomic hydrogen binds to this site with the formation of a 'surface hydroxide' with a typical bond length of 1 Å. In a first stage, the singly occupied H $1s$ state interacts with the oxygen $2p$ states, which are nearly fully occupied (the O atoms are formally in the O^{2-} configuration). This leads, initially, to the double occupation of the bonding combination and single occupation of the anti-bonding combination. If the transition metal oxide is of 'irreducible' character, the resulting OH^{2-} configuration would be the electronic ground state. For 'reducible' transition metal oxides, however, the surplus electron is transferred to the metal d states (see Figure 4.2). In the case of

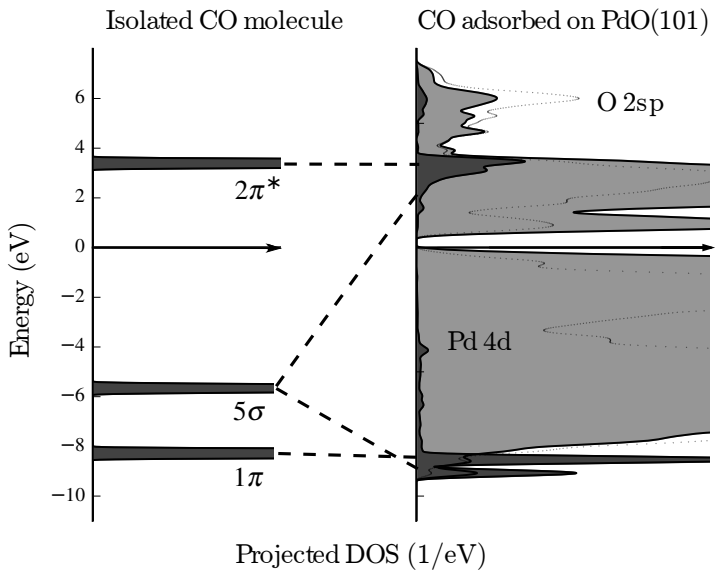

Figure 4.4: Density of states calculated with the HSE06 functional for atop-adsorbed CO on PdO(101). Left: the density of states in the isolated CO molecule. Right: the density of states projected on the CO s, p, Pd $4d$ and O s, p states when CO is adsorbed atop a threefold Pd atom in a PdO(101) slab.

PdO(101), a nearest-neighbour undercoordinated Pd atom is formally reduced from the +2 to the +1 oxidation state. The situation is analogous to other reducible oxides such as CeO_2, where H adsorption leads to the formation of Ce^{3+} ions [194].

4.3 Trends in catalytic activity

As for the case of the binding of surface species, qualitative concepts may help to explain and predict trends in the catalytic activity of different materials. For this purpose two components are needed. Firstly, it is required to known how to relate variations in the free energies of the relevant stable surface species and transition states to variations in the turnover rate (under the reaction conditions of interest). To this end, one may employ either e.g. full microkinetic simulations [195] and/or degree of rate control considerations [196]. Secondly, one should understand how the above free energies vary from one material to the next. Preferably, these variations can be correlated to one or two independent 'descriptors' (such as the d-band center from the previously mentioned d-band model).

In such 'scaling relations' often linear relationships are found between the descriptor and adsorption and activation energies.

This approach has thus far been successful in understanding the overall activity trends of transition metals for processes such as CO oxidation and NH_3 synthesis [197]. This is to a large extent made possible thanks to adequate mechanistic insight and because the *d*-band model explains the existence of scaling relations on transition metal surfaces [198, 199]. Activity trends for metal oxide catalysts, however, are generally less well understood. This appears to be caused, at least in part, by a greater variety in terms of reaction networks and bonding mechanisms. Scaling relations on metal oxide surfaces have so far only been observed for a limited number of cases, such as between O and OH adsorption energies [199–201]. Regarding methane activation, the energy for the radical-like methane dissociation transition state is known to be related to the H adsorption energy [202], which is in turn connected to the reducibility of the metal oxide [203]. For the surface-stabilized transition state, however, a similar relationship cannot be constructed because the adsorption energies of H and CH_3 do not show reliable scaling [204]. A linear correlation does appear when the transition state energy is compared to the final state energy where H and CH_3 are coadsorbed [204]. The scatter is, however, significant: the barrier for methane dissociation on the PdO(100) surface, for example, deviates from this relationship by 0.7 eV [205, 206]. The surface chemistry of metal oxides hence continues to be a challenging topic.

Chapter 5

Methane oxidation over PdO(101)

This chapter offers an introduction to methane oxidation over palladium and summarizes the parts from the appended papers that relate to the chemistry of the studied surface reactions. Methodological aspects contained in the appended papers are addressed separately in Chapter 6.

5.1 Previous research

The slow rate for the total oxidation of methane at low temperatures is mainly a kinetic problem. Thermodynamically, the process is favoured by a combustion enthalpy of over 9 eV per molecule [207], but the symmetry and the strengths of the C-H bonds can make the methane molecule difficult to activate. The issue of catalyzing this process has a long scientific tradition, dating back to the early twentieth century [208]. Specific interest in the platinum group metals rose in the sixties [209, 210]. In particular, palladium-based catalysts were discovered to have high activities under oxidizing conditions, whereas platinum is better suited under reducing conditions. For an extensive overview of palladium-based catalysts for methane oxidation, the reader is referred to a review by Ciuparu and coworkers [6].

Over the past decade, a consensus has grown that palladium is active both in a metallic and an oxidized form, and that the actual active phase depends on the reaction conditions [6, 206, 211, 212]. Palladium oxide seems to be the active form at moderate temperatures (below circa 950 K) and net oxidizing conditions. At higher temperatures and/or reducing conditions, the oxide is unstable and metallic palladium becomes the active material.

In the last years, further advances have been made regarding the activities of the different surface terminations of palladium oxide. DFT calculations indicate that the PdO(100) orientation is the thermodynamically stable surface termination of the bulk oxide, followed by the PdO(101) orientation [213] (see Figure 5.1 for structural models of these surface terminations). The difference in surface free energy between the two surfaces amounts to circa 30 meV/Å^2 at 600 K and an oxygen pressure of 1 atm [213]. There is also experimental evidence that the (100) orientation is the preferred surface

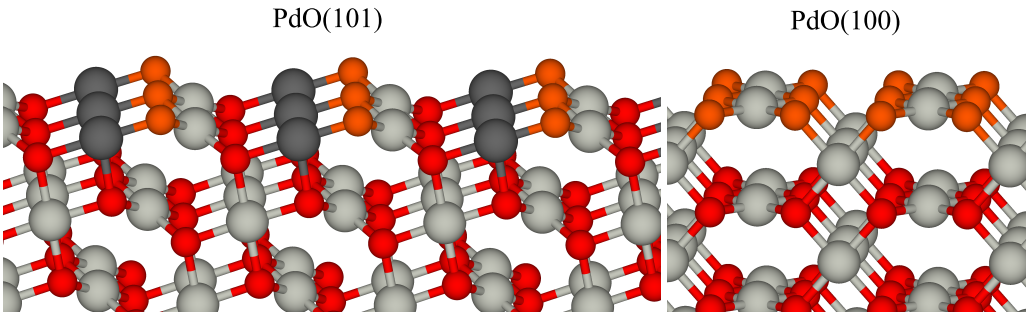

Figure 5.1: Ball-and-stick models of the PdO(101) and PdO(100) surfaces. The fourfold coordinated Pd and O atoms are coloured in respectively light gray and red. The threefold coordinated Pd and O atoms at the surface are given dark gray and orange colours.

orientation from bulk PdO [214–217]. It is therefore surprising that the (101) orientation has been observed experimentally on e.g. Pd(100) [206, 218]. This can be explained by the small lattice mismatch between PdO(101) and the Pd(100) substrate, which makes it the most favourable orientation, at least for film thicknesses up to four PdO layers [65]. High-quality PdO(101) thin films can also be grown on Pd(111) by exposure to an atomic oxygen beam in ultrahigh vacuum, followed by annealing [219]. The formation of the oxide is preceded by a Pd_5O_4 ($\sqrt{6} \times \sqrt{6}$) surface oxide on Pd(111) [104, 220] (see Figure 5.2).

Owing to the stability of the methane molecule, the dissociative adsorption of methane is typically considered to be a rate-determining step in the methane oxidation process. Theoretical investigations of the PdO(100) surface suggest that methane dissociation occurs with rather large energy barriers (1 eV or more) on this surface [206, 222]. The PdO(101) surface, on the other hand, displays much lower barriers for the initial dissociative adsorption (circa 0.5 eV with the PBE functional [206, 223, 224]). Importantly, the PdO(101) surface has been observed to be present during oxidation using in situ surface X-ray diffraction [206].

The topmost Pd atoms are coordinated differently on PdO(100) and PdO(101). On PdO(100) (see Figure 5.1), the surface Pd atoms are coordinated to a rectangle of four neighbouring O atoms. In this configuration, the Pd d_{z^2} orbitals are less involved in the bonding with the O atoms compared to the other d-orbitals. This results in a high occupation of the d_{z^2}, which upon adsorption yields a repulsion towards the σ-type MOs on the methane molecule. The PdO(101) surface, however, contains threefold coordinated O and Pd atoms at the surface (Figure 5.1). Due to the different arrangement of O atoms around the threefold Pd atom, in particular the presence of an O atom directly below

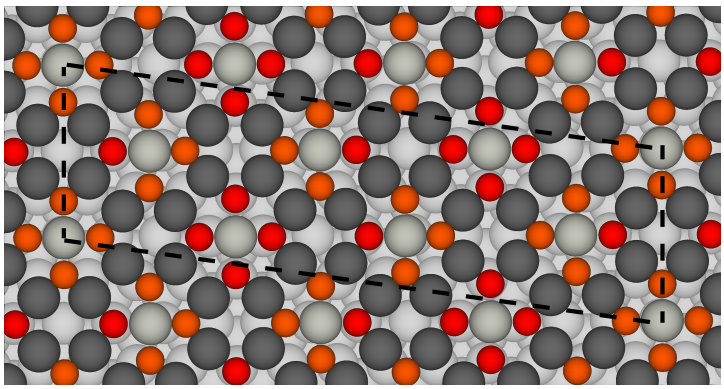

Figure 5.2: Structural model of the Pd_5O_4 ($\sqrt{6} \times \sqrt{6}$) surface oxide on Pd(111). The twofold and fourfold coordinated Pd atoms of the surface oxide are coloured in dark and light gray, respectively. The threefold and fourfold coordinated O atoms are coloured as orange and red.

the Pd atom, there is now a significant depopulation of the d_{z^2} states. This reduces the repulsion towards the methane molecule [206].

In view of the significance of the PdO(101) surface, the interaction of various reagents with the surface has previously been investigated [225]. Temperature programmed desorption (TPD) experiments in combination with DFT calculations have for example shown that water strongly adsorbs on the undercoordinated Pd atoms and can dissociate with the formation of Pd-OH and O-H species [226]. Calculations indicate that also CO shows strong affinity for the surface Pd atoms CO [218, 227]. Species that are more weakly adsorbed on the undercoordinated Pd sites include O_2 [228], CO_2 [229] and small alkanes such as methane, ethane and propane [223, 224, 230–233].

However, there is still an incomplete understanding of various aspects of the methane oxidation process over PdO(101). One question, for example, is the precise bonding configuration of intermediates to the surface, such as hydrogen and carbon monoxide. Moreover, the knowledge is limited concerning the subsequent pathways once methane is adsorbed and dissociated on the surface. Also the variation of the methane oxidation rate as a function of reaction conditions (i.e. the temperature and the gas-phase pressures of CH_4, O_2 and H_2O) is not yet well understood in terms of elementary surface reactions. These are the types of questions addressed in this thesis.

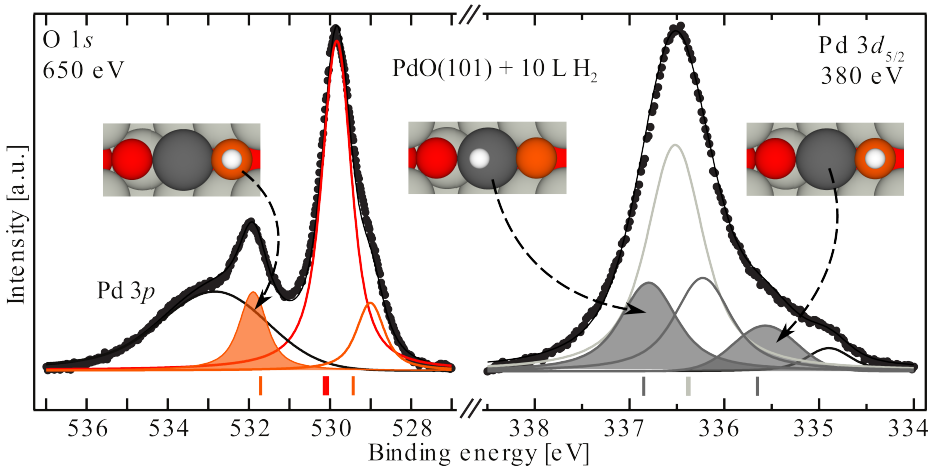

Figure 5.3: Measured core-level spectra from the O 1s (left) and Pd 3$d_{5/2}$ regions. The calculated CLS with respect to bulk atoms are indicated by the lines underneath each spectrum. The new surface components that arise after H_2 exposure are shaded and are connected to the matching surface species.

5.2 Hydrogen adsorption

In **Paper I**, the interaction of the PdO(101) surface with molecular hydrogen is investigated. Experimentally, the prepared PdO(101) sample was cooled down to liquid nitrogen temperatures (circa 110 K) in high vacuum and subsequently exposed to 10 Langmuir H_2. Pd 3d and O 1s core-level spectra were recorded before and after exposure. Computationally, various reactions of H_2 with the surface were explored, i.e. adsorption on threefold Pd sites, followed by dissociation and possible water formation. Comparing the measured and calculated Pd 3d and O 1s core-level shifts (CLS) reveals that hydrogen indeed dissociates to form Pd-H and O-H species, as shown in Figure 5.3. As mentioned previously in Chapter 4, the formation of O-H species leads to a reduction of the nearest-neighbour threefold Pd atom, which explains the shift to lower Pd 3d binding energies. The calculated energy barriers show that while H_2 dissociation is facile, relatively high energy barriers need to be overcome for the formation of water. This explains why water formation and reduction of the oxide surface is observed only at higher temperatures.

5.3 Carbon monoxide adsorption

A similar approach is used in **Paper II** for the adsorption of CO. In addition, infrared spectroscopy data was measured and calculated in order to obtain complementary

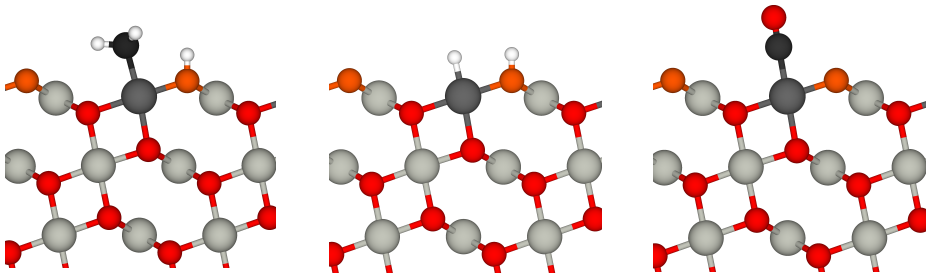

Figure 5.4: Ball-and-stick models of dissociatively adsorbed CH_4 and H_2 (left and center) and molecularly adsorbed CO (right) on the PdO(101) surface. The PdO atom colours are as in Figure 5.1. The additional C and H atoms are coloured in black and white, respectively.

information. Theoretically, the most favourable adsorption sites for CO are the sites atop and bridge with respect to the threefold Pd atoms. Comparing the measured and computed CLS and vibrational frequencies, it appears that both atop- and bridge-bound CO is present, with a majority of the former (see Figure 5.4).

Also CO adsorption on the Pd(111) surface and the $(\sqrt{6}\times\sqrt{6})$ Pd_5O_4 surface oxide on Pd(111) are considered in **Paper II**. An interesting aspect that is only briefly mentioned in the paper is the difference in the bonding of CO on the different surfaces. The CO adsorption energy in the atop sites on Pd(111) and PdO(101) are quite comparable (-1.38 eV and -1.49 eV, respectively, using the PBE functional). The charge difference plots shown in Figure 5.5, however, show that the origin for the strong binding to the oxide surface is different than on the metal. On the PdO(101) surface, there is significant charge accumulation between the palladium and carbon atoms, indicating stronger 5σ donation as compared to the metal (see Chapter 4). This compensates for the reduced backdonation to the CO $2\pi^*$ MO. Adsorption on the surface oxide, however, is clearly weaker (-0.59 eV), which is also visible from the lower charge transfer. Here, the lack of underlying O atoms lead to insufficient depletion of Pd s and d_{z^2} states, which increases the repulsion towards the CO molecule.

5.4 Methane oxidation

Paper III features a combination of experimental and theoretical work regarding the methane oxidation reaction over PdO(101). Starting from a Pd(100) single crystal surface, the temperature is raised from circa 440 K to 770 K in the presence of a 5:2 CH_4:O_2 gas mixture with a total pressure close to 1 mbar. Below 560 K, the O 1s and Pd 3d core-level spectra are characteristic of the $(\sqrt{5}\times\sqrt{5})-R27^\circ$ surface oxide over Pd(100). Structurally, this surface oxide is equivalent to a single PdO(101) layer on Pd(100). The CO_2 partial

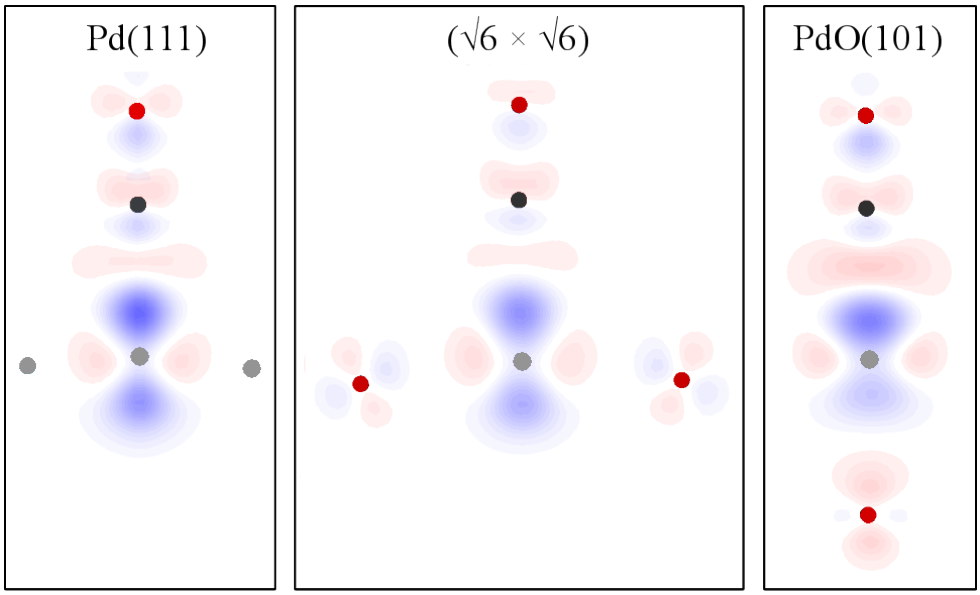

Figure 5.5: Charge density difference plots for CO adsorbed on atop sites of the Pd(111) surface, the $(\sqrt{6} \times \sqrt{6})$ surface oxide on Pd(111) and the PdO(101) surface. Red and blue regions represent charge accumulation and depletion, respectively.

pressure measured by mass spectrometry is very low, indicating that the surface oxide possesses much lower catalytic activity for CH_4 oxidation. When the temperature is raised further, the core-level signature of the PdO(101) surface emerges and the catalytic activity increases.

The difference between the single-layer surface oxide and the multi-layer PdO(101) surface can again be related to the local atomic structure. In the surface oxide, the oxygen atoms underneath the undercoordinated Pd atoms are absent, leading to an increase in the d_{z^2} states compared to the Pd atoms of the PdO(101) surface (see Figure 5.6). The resulting repulsive effect is visible in the higher electronic energy barrier for dissociation (1.34 eV versus 0.68 eV, using the PBE functional) and in the potential energy diagram for methane approaching the surface (see Figure 5.6).

In **Paper IV**, hybrid density functional theory and transition state theory are used to build a detailed kinetic model that describes the complete oxidation of methane over the PdO(101) surface. This model offers answers to several questions regarding the full reaction pathway of the methane oxidation process and its kinetic behaviour.

The high-temperature (T > 700 K) pathway for the conversion of methane is shown in Figure 5.7. The methyl species produced by the dissociative adsorption of methane

further react with the undercoordinated oxygen atoms, with CH_2, CH_2O, CHO and CO as main intermediates. Oxygen is mainly incorporated into the molecule through reaction with oxygen atoms of the substrate, which supports a Mars-van Krevelen mechanism. The catalytic cycle is completed by reoxidation of the oxygen vacancies by O_2 adsorption and dissociation. Water production occurs through reactions between surface hydroxyl groups. According to the model, the mechanism is slightly different at lower temperatures (600-700 K), where CH_3 preferably reacts with adsorbed O and further C-H dissociation steps mainly occur by reaction with adsorbed OH. Additionally, a second pathway for the dissociative adsorption of methane starts to contribute under these conditions, namely a route where methane reacts with the relatively abundant OH species, producing CH_3 and H_2O.

Interestingly, there appear to be strong attractive interactions between several species adsorbed on threefold Pd sites (such as CH_3, CH_2, CHO and OH) and H atoms adsorbed on threefold O sites. These interactions are on the order of 0.5 to 1 eV, which is large compared to the thermal energy. This means that the mean-field approximation is no longer valid. The adsorbates are not uniformly distributed over the surface, i.e. their positions become correlated. The concentration of CH_3-H pairs during methane oxidation, for example, is several orders of magnitude higher than the concentration expected from the mean-field approximation. In **Paper IV** this is resolved through a quasi-chemical approach, where e.g. the CH_3 species are treated separately depending on whether or not they are paired with a H species.

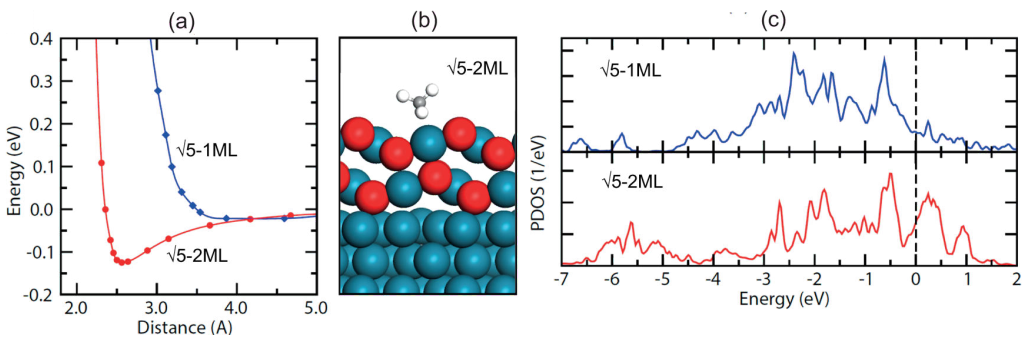

Figure 5.6: (a) Potential energy curves for CH_4 approaching the single and double ($\sqrt{5} \times \sqrt{5}$) oxide layers on Pd(100). (b) Structural model for CH_4 adsorbed on the two-layer PdO(101) surface oxide on Pd(100). (c) The density of states projected on the d_{z^2} states of the undercoordinated Pd atoms of the single and double ($\sqrt{5} \times \sqrt{5}$) oxide layers.

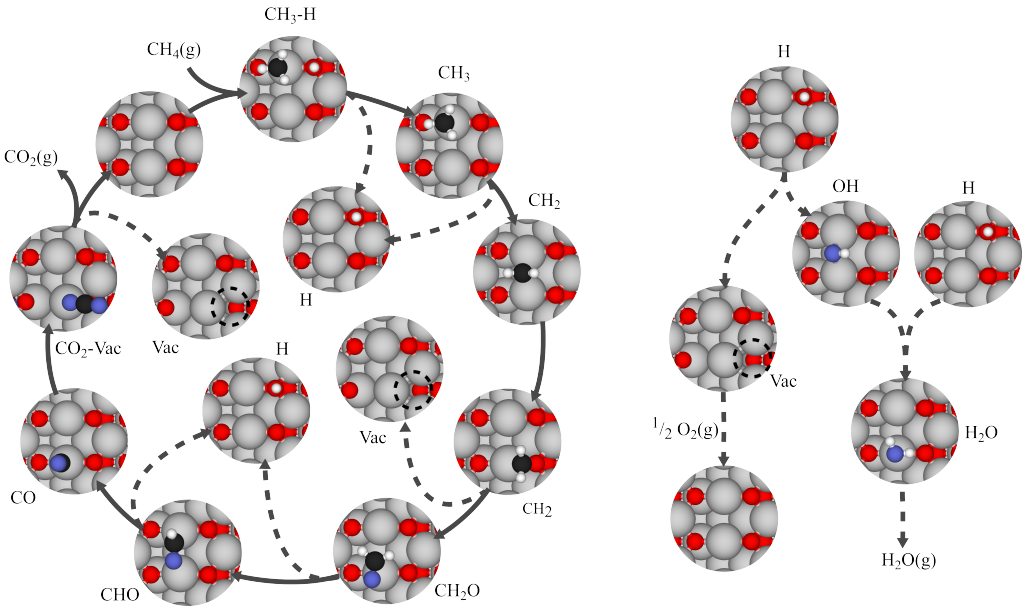

Figure 5.7: The main reaction pathway for the conversion of methane to carbon dioxide and water over the PdO(101) surface at moderate to high temperatures. Full arrows indicate the carbonaceous intermediates, whereas dashed arrows show the creation of other surface intermediates. Colour code as in Figure 5.4 and with adsorbate oxygen atoms in blue.

Several interesting results are also obtained regarding the kinetic behaviour of the methane oxidation process. The dissociative adsorption of CH_4, for example, appears to be partly reversible under certain conditions. This is due to the relatively slow decomposition pathways for the adsorbed CH_3 species. The stability of these species is further enhanced by the attractive interaction between the CH_3 and H species. This phenomenon offers an explanation for the observed below-unity reaction orders in CH_4 pressure at high temperatures. As the methane pressure is raised, the concentration of H species increases, which traps a higher portion of the CH_3 species into CH_3-H pairs. This, in turn, leads to a higher fraction of the methane molecules redesorbing before further oxidation can occur. Reaction orders of 0.6-0.7 have been measured experimentally [212], and values of 0.8-0.9 are predicted by the kinetic model.

Pairing effects can also explain the variation in measured apparent activation energies in the mid to high temperature regimes. Above 750 K and at pressures in the Torr range, a low apparent activation energy of circa 0.3 eV has been observed [212]. In **Paper III** a value of circa 0.7 eV is measured at temperatures between 650 and 750 K and pressures in the mbar

range. In both cases, the model predicts that the surface is essentially clean with a small amount of surface hydroxyl groups as the most abundant surface species, in agreement with the core-level measurements in **Paper III**. The apparent activation energies from the kinetic model are 0.27 and 0.80 eV, respectively, in agreement with the experiments.

At temperatures below circa 700 K and in the presence of water vapour, the surface is mostly covered by molecularly and dissociatively adsorbed H_2O, which inhibits the reaction rate. This is in agreement with the negative order in water pressure observed experimentally under those conditions [234] and leads to a further increase in the apparent activation energy to circa 1.3 eV. The kinetic model is also able to capture the increase in the apparent activation energy, though only up to a value of 0.97 eV.

5.5 Adsorbate pairing

Attractive interactions between adsorbates have also been observed on other oxide surfaces, such as NO_x pairs on alkaline earth oxides [235, 236]. This phenomenon is known to be characterized by charge transfer between the adsorption sites, similar to redox reactions. In order to gain a better understanding of what determines the total pairing energy, this topic is studied in detail in **Paper V**. In this study, OH-H and NO_2-NO pairing energies are compared on a series of metal oxide surfaces, namely rocksalt BaO(100), rutile TiO_2(110), fluorite CeO_2(111) and tetragonal PdO(101). The geometries of the adsorbate pairs are shown in Figure 5.8 (the separate adsorbates adsorb in similar configurations). The stabilization by pairing is most pronounced on BaO(100) and weakest on PdO(101). For a given oxide surface, OH and H gain more energy upon pairing than NO_2 and NO.

In order to evaluate the different contributions to the total pairing energy, the adsorbate pairing process is decomposed into separate subprocesses related to (i) the intrinsic redox properties of the adsorbates (ii) classical electrostatic interactions between the charged species, and (iii) ionic relaxation effects. The analysis shows that each of these components is important in order to understand the total stabilization upon pairing and to explain the observed trends for the different adsorbate pairs and oxide surfaces. As a result, it is difficult to find simple descriptors for predicting the magnitude of the pairing energy.

Paper V also discusses the connection between adsorbate pairing and reactivity. The reaction energy for A-B addition, for example, will vary depending on whether e.g. A is paired to a third adsorbate C. The difference between the paired and unpaired cases is directly related to the difference in A-C and AB-C pairing energies. This highlights the importance of adsorbate pairing for reactions on oxide surfaces, which has also been discussed in **Paper IV**.

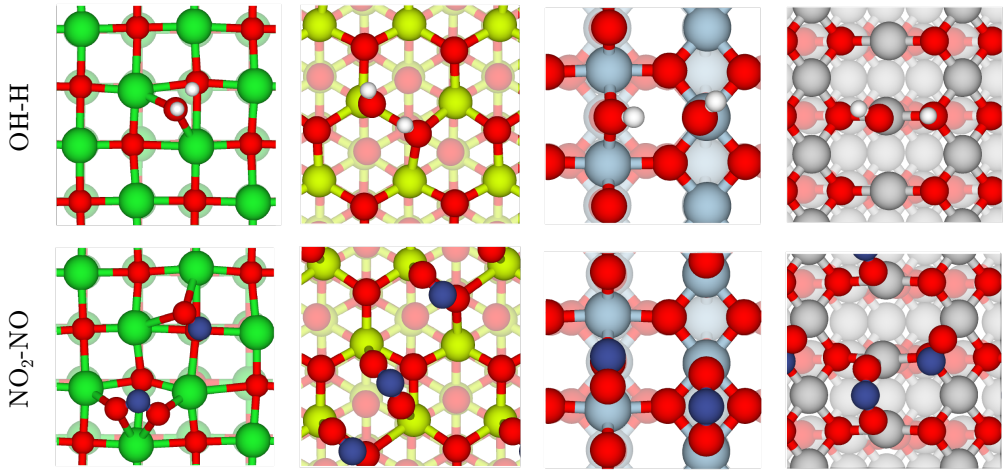

Figure 5.8: Top views of geometries of several adsorbates pairs, after ionic relaxation using the HSE06 functional. The atomic colour coding is: Ba (green), Ce (yellow), H(white), N (purple), O (red), Pd (gray), Ti (blue-gray).

5.6 Carbon monoxide oxidation

In **Paper VI** the attention turns to the effect of alloying Pd with Ag on the catalytic oxidation of the CO molecule. This is done by comparing the oxidation process over the Pd(100) surface with that over $Pd_{75}Ag_{25}(100)$. This is done in a temperature-programmed fashion, where the temperature is increased from around ambient temperature to several hundred degrees Celsius and back. Near-ambient-pressure XPS allows to follow the composition at the surface during the cycle, while the CO_2 production rate is monitored via mass spectrometry. The Pd(100) substrate shows the familiar hysteresis behaviour, where higher activity is observed during cooling than during heating. The hysteresis is caused by the kinetically hindered formation of the $(\sqrt{5} \times \sqrt{5})-R27^\circ$ surface oxide. In contrast to methane oxidation, where this surface oxide is rather inactive, its activity for CO oxidation is high and exceeds that of Pd(100) under the studied conditions. On $Pd_{75}Ag_{25}(100)$, however, the surface remains in a purely metallic state. Additionally, the direction of the hysteresis is now reversed.

The computational work in **Paper VI** focuses on investigating whether changes in the Pd/Ag ratio at the surface may explain the hysteresis reversal. For this purpose a mean-field microkinetic model is constructed, with oxygen and CO adsorption energies and O + CO activation energies obtained from DFT calculations with the PBE functional. These are evaluated at different Pd_xAg_{1-x} compositions of the top layer. Diffusion of Ag

between the top layer and the bulk is included in order to allow the surface Ag content to vary during the temperature program. Although the kinetic model is approximate in several ways, the reversed hysteresis on $Pd_{75}Ag_{25}(100)$ can be qualitatively reproduced. At sufficiently high temperatures, the adsorbate coverages are sufficiently low, which enables a partial Ag enrichment of the surface layer. The barriers for the O + CO reaction is increased at this new composition, and the catalytic activity decreases as a result.

5.7 Ideas for catalyst design

Even though PdO based catalysts display a remarkable activity for methane oxidation, the low-temperature activity leaves to be desired, especially in the presence of water vapour and sulfur oxides. Additionally, it would be advantageous to reduce the precious metal content of the catalyst. From the presented studies several clues can be extracted for the design of improved catalyst formulations.

- **Paper III** shows that the reactivity of the undercoordinated sites in PdO(101) is a local effect, arising from the particular arrangement of the oxygen ligands surrounding the Pd atom. This means that the PdO bulk could be replaced by a different material able to stabilize an ultrathin PdO layer with a similar Pd-O coordination.

  The search for such materials may for example be directed towards metal oxides with crystal structures similar to that of PdO. Unfortunately, the square or rectangular planar coordination of oxygen around a metal ion is relatively rare due to the close packing of the oxygen ions [237]. Only PtO, CuO, and certain other copper minerals are known to contain this type of coordination [237]. CuO is interesting in this respect, as the $Cu_xPd_{1-x}O$ mixed oxide adopts the PdO crystal structure for Cu fractions up to 72.5% [238].

  Also oxides with a different crystal structure may be considered. One interesting example in this direction is the $MgAl_2O_4$ spinel. When used as a support material, this oxide has been found to allow for epitaxial growth of a highly active, crystalline PdO phase [239].

- Another consequence of the ligand effect is that the undercoordinated Pd atoms at the surface may be replaced by other transition metals. This idea has been explored in Ref. [205], where the barriers for methane dissociation have been calculated on the (101) surface of the (real or hypothetical) tetragonal monoxides of Pd, Pt, Rh, Ir, Ag and Au. The barriers on PtO(101), IrO(101) and RhO(101) are found to

be relatively close to the barrier on PdO(101). The coinage metal oxides present higher barriers, in accordance with the understanding that σ-type orbitals increase the repulsion towards methane. The previously mentioned CuO is therefore most likely restricted to the potential role of support material, rather than providing sites for methane dissociation. Bimetallic Pd-Pt catalysts have previously been investigated, but it is uncertain whether Pt-doped PdO(101) surfaces are formed, as the PdO phase tends to segregate [240, 241]. **Paper VI** also shows that alloying may suppress the oxidation of the metal and that alloying elements may segregate under certain reaction conditions.

Nickel oxides may be interesting in this respect, as nickel lies one row above palladium in the periodic table. While the catalytic activity of NiO is low [210], the reactivity towards methane can be enhanced when nickel is in the (+3) oxidation state. A recent study shows promising results for nickel cobaltite ($NiCo_2O_4$) in terms of low-temperature activity in both presence and absence of water [242].

- From **Paper IV** can be deduced that the transition state for methane dissociation is not the only relevant design criterion for an active methane oxidation catalyst. In order to gain adequate low-temperature activity, the active sites need to show reduced sensitivity to water poisoning. One way to reduce the affinity towards water adsorption may be to increase the *s*-electron count on the transition metal atom, but this is likely to also increase the barrier for methane dissociation, as discussed in the previous paragraph. Adsorbed CH_3 species also display relatively high stability, indicating that efficient catalysts also need to provide sufficiently rapid CH_3 decomposition pathways. This may require consideration of the adsorbate pairing interaction between CH_3 and H species.

- It also appears that adsorbate pairing is important in the context of scaling relations. On transition metal surfaces, which do not exhibit adsorbate pairing, the barrier for the surface-stabilized dissociation of methane can be linearly correlated to the adsorption energy of either H or CH_3 [202]. On nonmetallic oxide surfaces, this relationship is no longer valid, and the adsorption energy of coadsorbed H and CH_3 needs to be employed instead [202]. This can be seen as a consequence of the complex character of adsorbate pairing, as exposed in **Paper V**.

When screening potential catalysts, it needs to be recognized that the free energy landscape for methane oxidation may be rather different as compared to PdO(101). Transition states and intermediates which display negligible degrees of rate control on PdO(101) may become influential on other surfaces.

Chapter 6

Reflections on computational methodology

This chapter offers a discussion of the methodological aspects contained in the appended papers. These include (i) the exchange-correlation functional dependence, (ii) local and global optimization methods, (iii) the calculation of partition functions, and (iv) kinetic modelling approaches.

6.1 Density functionals

In this thesis mainly the GGA functional PBE and the hybrid functionals PBE0 and HSE06 have been used. While the PBE functional is often considered a sensible choice for calculations involving metallic Pd, it has become clear that several properties of bulk PdO and the PdO(101) surface are not described satisfactorily by the PBE functional.

Regarding bulk PdO, experiments indicate semiconducting behaviour with a band gap of circa 1 eV [243, 244]. As mentioned in Chapter 2, (semi-)local functionals describe PdO as a metal, albeit with a small density of states at the Fermi level [245, 246]. A Kohn-Sham band gap close to the experimental value opens up when hybrid functionals such as PBE0 and HSE06 are used [65]. Also the Pd $3d$ shift between bulk Pd and bulk PdO is sensitive to the exchange-correlation functional. This is discussed in **Paper VII**, where the effect of HF exchange on the computation of CLSs is investigated. Using the PBE functional, this shift is underestimated by circa 0.7 eV. PBE0 and HSE06 single-point calculations at the PBE geometry yield better agreement with experiment, though the PBE underestimation tends to be overcorrected when 25% of HF exchange is used. In **Paper VII** the functional dependence is attributed, in part, to the slight increase in the Pd-O charge separation upon admixing the HF exchange. Similarly, also the C $1s$ CLSs in the ESCA molecule (ethyl trifluoroacetate) are found to be better described with PBE0 than with PBE due to an increased C-O and C-F charge separation in the initial state. These effects can be attributed to a reduction of the self-interaction error, which leads to more favourable charge accumulation on electronegative elements.

Concerning the chemical properties of the PdO(101) surface, there are also several indications that hybrid functionals generally improve on the generalized-gradient approximation. Experimentally it has been found that CO adsorbs mainly atop of undercoordinated Pd atoms, with a large O 1*s* shift with respect to the bulk oxide. The preference for the atop position and the magnitude of the O 1*s* shift is is better reproduced with PBE0 than with PBE (see **Paper VII**). Molecular adsorption of O_2 to the undercoordinated Pd sites is also sensitive to the exchange-correlation treatment (see **Paper IV**). Compared to temperature programmed desorption (TPD) measurements [225, 228], the PBE functional leads to a significant overbinding of the O_2 molecule, whereas the adsorption energy is much reduced using HSE06. This difference has a marked effect on the description of the complete CH_4 oxidation reaction: at low temperatures PBE will predict surface poisoning by molecular oxygen, whereas HSE06 gives the experimentally observed site blocking by water. Judging from the apparent activation energy at high temperatures, also the barrier for CH_4 dissociation appears to be better described by hybrid functionals.

Exchange-correlation dependencies are also addressed in **Paper V** in the context of OH-H and NO_2-NO pairing on BaO(100), TiO_2(110), CeO_2(111) and PdO(101). The adsorption of OH and NO_2 on cationic sites is typically significantly less exothermic with HSE06 as compared to PBE, The adsorption of H and NO, on the other hand, is typically more exothermic in HSE06. Also OH-H and NO_2-NO pairing energies are generally more exothermic using the hybrid functional. This functional dependence is not only of electronic origin, but includes significant contributions from ionic relaxation. It is hence not always sufficient to perform hybrid functional single-point calculations at the PBE geometries. This appears to be most pronounced in the case of the open-shell molecules on the surfaces other than PdO(101). Unfortunately, there are currently no experimental measurements nor high-level wavefunction calculations to which the two functionals can be compared. It is known, however, that hybrid functionals offer better descriptions of the localized Ti^{3+} and Ce^{3+} states (and associated polaronic distortions) as compared to GGA functionals where the defect states are delocalized over several cations.

Van der Waals interactions are usually considered to be relatively unimportant when dealing with small molecules that are covalently bonded to the substrate, and have therefore not been considered in this thesis. One exception, however, is made for the case of molecularly adsorbed water (see **Paper IV**). Using the Grimme dispersion correction [247] a van der Waals contribution of 0.2 eV is calculated to the total adsorption energy. This correction leads to an improved description of the water inhibition at low temperatures. A similar van der Waals contribution has also been found to bring the calculated adsorption energy of water on the CeO_2(111) surface in closer agreement with TPD data [248].

6.2 Local optimization

Local minimization can usually be executed in a straightforward manner when using the relatively inexpensive GGA functionals, starting e.g. from a hand-made guess for the geometry. Hybrid functionals, however, are more computationally intensive by several orders of magnitude, which calls for more careful approaches. The local minimizations using the HSE06 functional in **Paper V** are usually performed starting from the relaxed PBE geometry. In case significant distortions are expected to occur due to the formation of localized Ti^{3+} and Ce^{3+} states, the relaxed PBE+U geometry is used instead, with effective U values of 4-5 eV applied to the Ti d or Ce f states. In **Paper V** the cost of the local minimization is further limited by only including the Γ-point in the evaluation of the Fock operator. The full k-point mesh is only used in a single ground state calculation at the final geometry. Selected test cases, such as H adsorbed on $CeO_2(111)$, indicate that this approximation is suitable.

For transition state searches, such as the ones performed in **Paper VI** and **Paper IV**, the dimer method often proved more convenient than the more commonly used NEB method. As the reactant and product geometries are not needed, a reasonable guess for the transition state and the negative curvature mode is sufficient. Although the dimer method can require more force calls to converge to the saddle point, it can still result in a reduced computational cost thanks to the reduced number of structures. This is particularly the case when the minimum energy path is long and many intermediates are needed in the NEB method. One example where this problem may arise is the reaction of surface species with formation of a product in the gas phase.

6.3 Global optimization

During this thesis work also the problem of global structural optimization has been investigated. One example where this problem arises in the context of computational catalysis is the structure of surface oxides on transition metal surfaces. In order to evaluate and develop genetic algorithms for such structures, the $Pd_{10}O_8$ surface oxide on Pd(111) is used as a test case. The structure of this surface oxide on was originally found through simulated annealing [104], requiring on the order of 10^5 force calls.

When the potential energy landscape is described using a ReaxFF potential [249], the global minimum is not the real $(\sqrt{6} \times \sqrt{6})$ structure but a lower symmetrical structure containing two- and threefold coordinated Pd atoms (see Figure 1). Three ways have been found so far to improve the performance of the standard ASE-GA code for the $Pd_{10}O_8$ surface oxide case. Firstly, the effect of decoupling the pairing and crossover

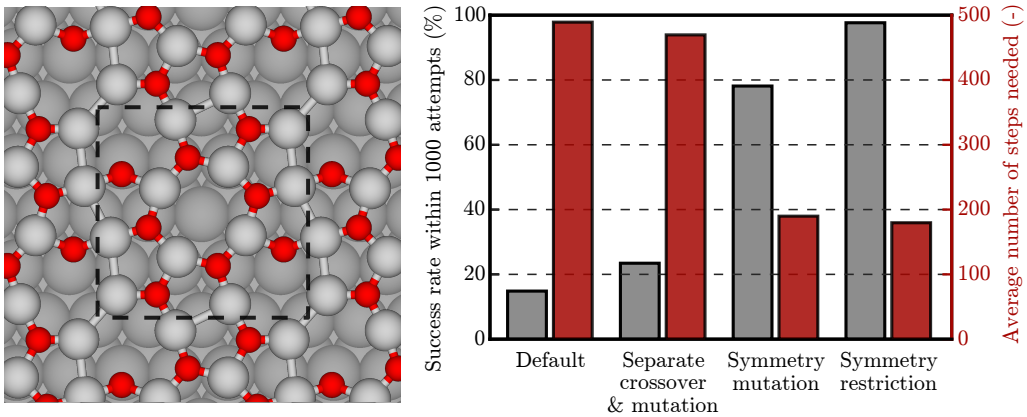

Figure 6.1: Left: global minium for the $Pd_{10}O_8$ surface oxide layer on Pd(111) using the ReaxFF potential. Colour code: Pd (light), O (dark). Right: average success rates (gray) and required number of GA iterations for retrieving the global minimum using different GA implementations. In each version, 90% (10%) of the candidates are created by crossover (mutation).

operations is investigated. By default, it is suggested to apply mutations after a structure has been generated from a crossover operation, but before undergoing local optimization [250]. Mutating already relaxed structures is however found to be more effective. Figure 6.1 shows that this leads to a higher success rate compared to the default case, without increasing the average number of steps required to retreive the global optimum.

The other two improvements aim to take advantage of a priori knowledge about the symmetry of the target structure. This can be useful because stable structures often display symmetry and because such knowledge is often more readily available than the full geometrical structure. The ReaxFF global minimum possesses the *p2* plane symmetry, with a subset of the atoms displaying *p4* symmetry. Firstly, a mutation is designed that symmetrizes an existing structure to a mixture of *p2* and *p4* symmetries. Secondly, a entirely symmetry-restricted GA is constructed, where only *p2*-symmetrical structures are considered and where the symmetry is conserved by the genetic operators and the local optimization procedure. Figure 6.1 shows that both approaches allow to further improve the success and convergence rates of the algorithm.

Currently ongoing work indicates that the above findings also apply when the potential energy landscape is described by the PBE functional. Using the same $Pd_{10}O_8$ unit on a two-layer Pd(111) slab, the $\sqrt{6}$ structure is found after circa 50 iterations of the algorithm on average, requiring circa $5 \cdot 10^3$ force calls on average. The employed genetic algorithm (described in Chapter 3) uses a population of 20 structures and a typical set of

genetic operators (80% cut-and-splice operator, 10% O-Pd permutations and 10% rattle mutation). The initial random structures are generated with *p4* symmetry (scanning tunneling microscopy images show that the structure has *p4mm* symmetry).

6.4 Partition functions

In **Paper IV** also the pre-exponential factors of the rate coefficients are evaluated from first principles. It is often a point of discussion how this evaluation should be performed, in particular which statistical mechanical model (such as the quantum harmonic oscillator (QHO), the free or hindered translator, the rigid rotor, ...) should be used to describe the partition function of a given eigenmode. The guiding principle, however, is rather clear: the model should be a faithful representation of the part of the potential energy landscape (PES) that is relevant at the temperature of interest. If the calculated eigenenergy exceeds the thermal energy (e.g. 60 meV at 700 K), the relevant part of the PES can be considered harmonic, such that the QHO model is appropriate. This is the case for the vast majority of the encountered eigenmodes. When lower eigenenergies are observed, more information about the PES is needed. In **Paper IV**, this is done by searching for the appropriate transition state in the direction of the eigenmode. Molecularly adsorbed H_2O atop undercoordinated Pd atoms, for example, displays a low-curvature mode for translation along the undercoordinated Pd rows. The barrier for diffusion along this direction is found to be large compared to the thermal energy, implying that the QHO model is more appropriate than the free or hindered translator models. Another example is the rotation of CH_3 adsorbed H_2O atop undercoordinated Pd atoms along the Pd-C axis. In this case, the associated eigenenergy as well as the barrier for rotation are low compared to the thermal energy, so that the rigid rotor model is more appropriate.

6.5 Kinetic modelling

As shown in **Paper IV** and **Paper V**, adsorbates on metal oxide surfaces may experience attractive interactions. Particularly relevant for methane oxidation over PdO(101) is the electronic pairing between CH_3 and H adsorbed on undercoordinated Pd and O atoms, respectively. As the calculated stabilization can be very pronounced (up to 1 eV), it is clear that the mean-field approximation will be in error. This is illustrated in Figure 6.2 for the case of a one-dimensional array of site pairs comparable to the PdO(101) surface. As the pairing between the adsorbates becomes more exothermic, the mean-field approximation severely underestimates the coverage of adsorbate pairs on the surface. This effects becomes increasingly pronounced as the adsorbate coverage decreases.

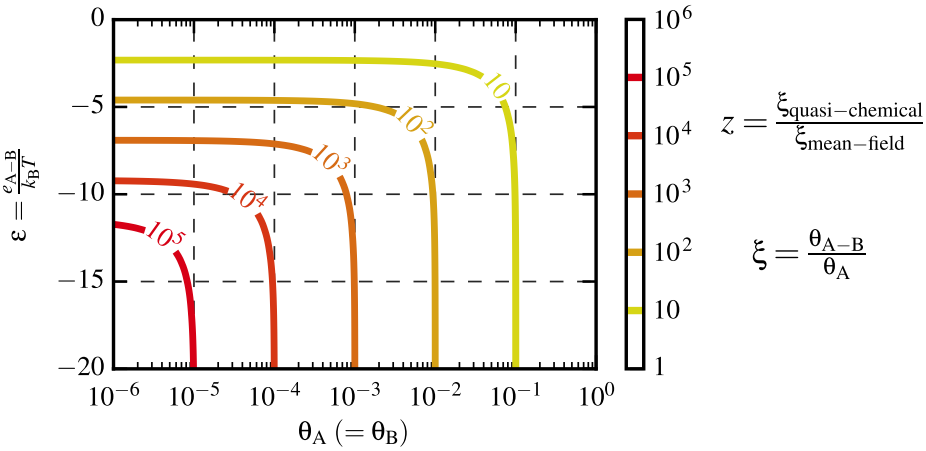

Figure 6.2: Ratio of the exact relative coverage of adsorbate pairs (ξ_{exact}) to the corresponding mean-field result ($\xi_{mean-field}$), as a function of the adsorbate coverage θ_A ($=\theta_B$) and the attractive A-B interaction strength ε.

In the quasi-chemical approximation the spatial correlations between the adsorbates on the PdO(101) are described more accurately (see Chapter 2). One remaining assumption, however, is that surface diffusion is relatively fast, so that the distribution of an adsorbate into paired and unpaired states is given by thermodynamic equilibrium. It would be interesting to evaluate this approximation by resolving the barriers for diffusion and simulating the reaction kinetics using kinetic Monte Carlo methods.

Chapter 7

Conclusions and outlook

The main objective of this thesis has been to reach a detailed understanding of catalytic methane oxidation over the PdO(101) surface. This has been done by investigating the elementary surface reactions that occur when methane and other reactants interact with the surface. The used methodology is based on first-principles calculations using density functional theory (DFT), with different connections to experiments.

Several steps towards the objective have been achieved. By combining DFT calculations with photoemission measurements, it is shown that PdO(101) provides sites for adsorption of H_2 and CO. H_2 dissociates easily to form H atoms bound to undercoordinated Pd and O atoms, whereas adsorbed CO is mainly found on top of the undercoordinated Pd atoms of the surface. Additionally, the important role of the oxygen atoms below the undercoordinated Pd atoms for methane oxidation is shown in a joint theoretical and experimental study. The ligand effect on the local electronic structure at the undercoordinated Pd surface atoms effectively explains the difference in activity between single- and multilayer PdO(101) thin films on Pd(100).

This work also contains an investigation of the full reaction mechanism by which methane is converted into carbon dioxide and water over the PdO(101) surface. A detailed kinetic model of this mechanism has been constructed that is able to describe many features of the methane oxidation kinetics in terms of of elementary reactions on the PdO(101) surface.

Lastly, methodological contributions are made that highlight the sometimes limited accuracy of gradient-corrected density functionals in calculating reaction energies, energy barriers and core-level shifts involving the PdO(101) surface. Hybrid functionals are found to generally provide an improved description of these properties, though at a considerable additional computational cost.

In conclusion, the present work shows that it is possible to follow surface reactions and identify adsorbed species on palladium oxide surfaces by combining DFT calculations and carefully controlled experiments (most notably core-level spectroscopy). The combination of theory and experiment proved to have symbiotic effect. On one hand, the calculations have assisted in the interpretation of the experiments. On the other hand, the experimental

measurements have made it possible to evaluate the theoretical methodology. In this way, these combined studies have contributed to the understanding of the different types of binding sites on, in particular, the PdO(101) surface, as well as to progresses in the employed computational methodology. These two contributions, in turn, have allowed the subsequent construction of a detailed theoretical model for the oxidation of methane.

7.1 Next steps

Currently ongoing work aims at further extending the kinetic model for methane oxidation over PdO(101). The reaction network, for example, is being expanded to include surface reactions relevant to low-temperature poisoning by CO_2. Preliminary results indicate that site blocking by HCO_3-H pairs is responsible for this effect. Also the possible influence of transport limitations will be examined by coupling the microkinetic simulations to a model for pore and film transport. Additionally, the activity of oxidized versus metallic Pd for methane oxidation will be revisited in a combined experimental and theoretical study. Experimental reaction rates on metallic and oxidized Pd foil will then be compared to calculated turnover frequencies on Pd(100) and PdO(101).

Another current line of research involves the development and application of genetic algorithms for resolving surface structures. Alternative pairing and mutation operators are being considered, as well as strategies to take advantage of the presence of symmetry. A second computational topic will be to assess the performance of Perdew-Zunger self-interaction-corrected functionals for adsorption properties of metal oxide surfaces. Lastly, charged supercell correction schemes are being implemented to enable the study of charged adsorbates on insulating surfaces. This would allow the computation of e.g. the dilute-limit ionization potentials, electron and proton affinities and core-level shifts of adsorbates in a periodic electronic structure code.

7.2 Outlook

The results obtained so far have several implications. The detailed understanding of the different elementary surface reactions and their kinetic properties, for example, can provide inspiration for the design of new materials with improved catalytic activity. Also the advances in the understanding of the connection between the structure and the activity of the PdO(101) surface can be useful to this end.

Next, the methodological contributions have raised awareness about the limited accuracy of the generalized gradient approximation in the description of transition metal oxides such as PdO. This highlights the current need for density functionals which bring

DFT closer to chemical accuracy. To this end, also high-quality benchmark data are needed, which are presently lacking due to both theoretical and experimental difficulties. Reaction energies and activation energies on the PdO(101) surface may be a valuable component of such a future data set.

Furthermore, the work shows that care needs to be taken in modelling surface kinetics on insulating and semiconducting oxide surfaces, where the presence of strong adsorbate interactions leads to a breakdown of the mean-field approximation. This necessitates the use of methods that take into account the correlations between adsorbed particles. This information can also be of interest to experimental activity when kinetic parameters are deduced from reactor data.

Acknowledgements

The research presented in this thesis was carried out at the Division of Chemical Physics and the Competence Centre for Catalysis (KCK), Chalmers University of Technology, Göteborg, Sweden, during the period of October 2012 to February 2017.

The Competence Centre for Catalysis is hosted by Chalmers University of Technology and financially supported by the Swedish Energy Agency and the member companies AB Volvo, ECAPS AB, Haldor Topsøe A/S, Scania CV AB, Volvo Car Corporation AB and Wärtsilä Finland Oy.

The research has been funded by the Swedish Research Council (Vetenskapsrådet). Additional support has been obtained from the COST Action CM1104, the Åforsk foundation, and Chalmers Areas of Advance Transport and Nanoscience and Nanotechnology. CPU time has been granted by SNIC at C3SE (Göteborg) and PDC (Stockholm).

Additionally I would like to express my gratitude to:

My main supervisor Henrik Grönbeck, for your guidance, supportiveness, for the many discussions (often both serious and humorous at the same time) and for helping me both how to understand my results and how to communicate them. I also very much appreciate the freedom I received in handling the different projects, as well as the many opportunities to attend various international conferences. It has been a really productive, educational, and enjoyable time!

My co-supervisor Anders Hellman, for luring me into this PhD project. That circle is now complete! Thank you for helping me understand electronic structure theory, both through the computational physics course and by keeping the door open for any questions and discussions.

My main experimental collaborators – Natalia Martin and Edvin Lundgren. I have learned a lot from your experiments and our discussions.

The hosts of my research visits: Bjørk Hammer and Hannes Jónsson and their respective research groups in Aarhus and Reykjavik. In both places I enjoyed a very welcoming stay where I got exposed to many new methods and ideas.

My fellow members of the Chemical Physics group (current and past), for creating a both pleasant and stimulating atmosphere. In particular, I want to thank Adriana, Jakub, Oliver, Simon, Igor, Pooya, Anna, Chris, Adam, Mikael, Lin, Baochang, Matthias, Mikkel, Viktor, Michael, Unni, Arturo, and Alvaro.

My fellow KCK members (current and past), for showing the value of multidisciplinarity and maintaining the positive climate at the centre. Additional thanks for the good times go to Emma, Freddy, Mattias, Alexander, Sheedeh, Johan, Soran, Carl-Robert, Peter, and Ting.

Last, but not least, I'm very grateful for the continued support and encouragement I receive from my family and for the ways they have helped me to shape my interests.

Bibliography

[1] United Nations. *World Economic and Social Survey 2013: Sustainable Development Challenges*. 2013. URL: http://www.un.org/en/development/desa/publications/world-economic-and-social-survey-2013-sustainable-development-challenges.html.

[2] European Commission. *Europe 2020 A strategy for smart, sustainable and inclusive growth*. 2010.

[3] D. A. Lashof and D. R. Ahuja. *Nature* **344**, 6266 (1990), 529–531. DOI: 10.1038/344529a0.

[4] D. T. Shindell et al. *Science* **326**, 5953 (2009), 716–718. DOI: 10.1126/science.1174760.

[5] R. Kaufman and D. Stern. *Annual Estimates of Global Anthropogenic Methane Emissions: 1860-1994*. Tech. rep. 1998.

[6] D. Ciuparu et al. *Catal. Rev.s* **44**, 4 (2002), 593–649. DOI: 10.1081/CR-120015482.

[7] NGV Journal. *Worldwide NGV statistics*. URL: http://www.ngvjournal.com/worldwide-ngv-statistics (visited on 02/02/2015).

[8] Göteborgenergi. *GoBiGas meets the growing need for biogas*. URL: http://gobigas.goteborgenergi.se (visited on 02/02/2015).

[9] A. L. Polyzakis, C. Koroneos, and G. Xydis. *Energy Convers. Manage.* **49**, 4 (2008), 551–563. DOI: 10.1016/j.enconman.2007.08.002.

[10] R. P. Feynman. *Int. J. Theor. Phys.* **21**, 6-7 (1982), 467–488. DOI: 10.1007/BF02650179.

[11] P. Pyykko. *Chem. Rev.* **88**, 3 (1988), 563–594. DOI: 10.1021/cr00085a006.

[12] R. M. Martin. *Electronic Structure: Basic Theory and Practical Methods*. Cambridge University Press, 2004.

[13] L. H. Thomas. *Math. Proc. Cambridge* **23**, 05 (1927), 542–548. DOI: 10.1017/S0305004100011683.

[14] E. Fermi. *Rend. Accad. Naz. Lincei* **6**, 6 (1927), 602–607.

[15] P. Hohenberg and W. Kohn. *Phys. Rev.* **136**, 3B (1964), B864–B871. DOI: 10.1103/PhysRev.136.B864.

[16] W. Kohn and L. J. Sham. *Phys. Rev.* **140**, 4A (1965), A1133–A1138. DOI: 10.1103/PhysRev.140.A1133.

[17] G. B. Bacskay and S. Nordholm. *J. Phys. Chem. A* **117**, 33 (2013), 7946–7958. DOI: 10.1021/jp403284g.

[18] T. Koopmans. *Physica* **1**, 1–6 (1934), 104–113. DOI: 10.1016/S0031-8914(34)90011-2.

[19] J. P. Perdew and M. Levy. *Phys. Rev. B* **56**, 24 (1997), 16021–16028. DOI: 10.1103/PhysRevB.56.16021.

[20] J. P. Perdew and M. Levy. *Phys. Rev. Lett.* **51**, 20 (1983), 1884–1887. DOI: 10.1103/PhysRevLett.51.1884.

[21] E. J. Baerends and O. V. Gritsenko. *J. Phys. Chem. A* **101**, 30 (1997), 5383–5403. DOI: 10.1021/jp9703768.

[22] R. Stowasser and R. Hoffmann. *J. Am. Chem. Soc.* **121**, 14 (1999), 3414–3420. DOI: 10.1021/ja9826892.

[23] E. O. Jónsson et al. *J. Chem. Theory Comput.* (2016). DOI: 10.1021/acs.jctc.6b00809.

[24] M. Levy and J. P. Perdew. *Int. J. Quantum Chem.* **49**, 4 (1994), 539–548. DOI: 10.1002/qua.560490416.

[25] K. Burke, J. P. Perdew, and M. Levy. "Semilocal Density Functionals for Exchange and Correlation: Theory and Applications". *Theoretical and Computational Chemistry*. Ed. by J. M. S. a. P. Politzer. Vol. 2. Modern Density Functional TheoryA Tool for Chemistry. Elsevier, 1995, pp. 29–74.

[26] D. C. Langreth and J. P. Perdew. *Solid State Communications* **17**, 11 (1975), 1425–1429. DOI: http://dx.doi.org/10.1016/0038-1098(75)90618-3.

[27] O. Gunnarsson and B. I. Lundqvist. *Phys. Rev. B* **13**, 10 (1976), 4274–4298. DOI: 10.1103/PhysRevB.13.4274.

[28] J. Harris. *Phys. Rev. A* **29**, 4 (1984), 1648–1659. DOI: 10.1103/PhysRevA.29.1648.

[29] K. Burke. "Digging into the Exchange-Correlation Energy: The Exchange-Correlation Hole". *Electronic Density Functional Theory*. Ed. by A. J. F. Dobson, P. G. Vignale, and D. M. P. Das. Springer US, 1998, pp. 19–29.

[30] K. Burke, J. P. Perdew, and Y. Wang. "Derivation of a Generalized Gradient Approximation: The PW91 Density Functional". *Electronic Density Functional Theory*. Ed. by A. J. F. Dobson, P. G. Vignale, and D. M. P. Das. Springer US, 1998, pp. 81–111.

[31] M. Ernzerhof, K. Burke, and J. P. Perdew. "Density Functional Theory, the Exchange Hole, and the Molecular Bond". *Theoretical and Computational Chemistry*. Ed. by J. M. Seminario. Vol. 4. Recent Developments and Applications of Modern Density Functional Theory. Elsevier, 1996, pp. 207–238.

[32] J. C. Slater. *Phys. Rev.* **81**, 3 (1951), 385–390. DOI: 10.1103/PhysRev.81.385.

[33] J. P. Perdew and A. Zunger. *Phys. Rev. B* **23**, 10 (1981), 5048–5079. DOI: 10.1103/PhysRevB.23.5048.

[34] D. M. Ceperley and B. J. Alder. *Phys. Rev. Lett.* **45**, 7 (1980), 566–569. DOI: 10.1103/PhysRevLett.45.566.

[35] A. Ruzsinszky and J. P. Perdew. *Computational and Theoretical Chemistry* **963**, 1 (2011), 2–6. DOI: 10.1016/j.comptc.2010.09.002.

[36] M. Ernzerhof and G. E. Scuseria. *J. Chem. Phys.* **110**, 11 (1999), 5029–5036. DOI: 10.1063/1.478401.

[37] M. Swart, A. W. Ehlers, and K. Lammertsma. *Molecular Physics* **102**, 23-24 (2004), 2467–2474. DOI: 10.1080/00268970420002750 17.

[38] J. Sun et al. *Phys. Rev. B* **84**, 3 (2011), 035117. DOI: 10.1103/PhysRevB.84.035117.

[39] K. Burke, J. P. Perdew, and M. Ernzerhof. *J. Chem. Phys.* **109**, 10 (1998), 3760–3771. DOI: 10.1063/1.476976.

[40] R. O. Jones and O. Gunnarsson. *Rev. Mod. Phys.* **61**, 3 (1989), 689–746. DOI: 10.1103/RevModPhys.61.689.

[41] J. P. Perdew et al. *Phys. Rev. B* **46**, 11 (1992), 6671–6687. DOI: 10.1103/PhysRevB.46.6671.

[42] J. P. Perdew, K. Burke, and M. Ernzerhof. *Phys. Rev. Lett.* **77**, 18 (1996), 3865–3868. DOI: 10.1103/PhysRevLett.77.3865.

[43] Y. Zhao, N. González-García, and D. G. Truhlar. *J. Phys. Chem. A* **109**, 9 (2005), 2012–2018. DOI: 10.1021/jp045141s.

[44] S. Kurth, J. P. Perdew, and P. Blaha. *International Journal of Quantum Chemistry* **75**, 4-5 (1999), 889–909. DOI: 10.1002/(SICI)1097-461X(1999)75:4/5<889::AID-QUA54>3.0.CO;2-8.

[45] A. E. Mattsson et al. *J. Chem. Phys.* **128**, 8 (2008), 084714. DOI: 10.1063/1.2835596.

[46] J. P. Perdew and S. Kurth. "Density Functionals for Non-relativistic Coulomb Systems in the New Century". *A Primer in Density Functional Theory*. Ed. by C. Fiolhais, F. Nogueira, and M. A. L. Marques. Lecture Notes in Physics 620. Springer Berlin Heidelberg, 2003, pp. 1–55.

[47] Z. Wu and R. E. Cohen. *Phys. Rev. B* **73**, 23 (2006), 235116. DOI: 10.1103/PhysRevB.73.235116.

[48] F. Tran et al. *Phys. Rev. B* **75**, 11 (2007), 115131. DOI: 10.1103/PhysRevB.75.115131.

[49] J. P. Perdew et al. *Phys. Rev. Lett.* **100**, 13 (2008), 136406. DOI: 10.1103/PhysRevLett.100.136406.

[50] J. Tao et al. *Phys. Rev. Lett.* **91**, 14 (2003), 146401. DOI: 10.1103/PhysRevLett.91.146401.

[51] Y. Zhao and D. G. Truhlar. *J. Chem. Phys.* **125**, 19 (2006), 194101. DOI: 10.1063/1.2370993.

[52] J. Sun, A. Ruzsinszky, and J. Perdew. *Phys. Rev. Lett.* **115**, 3 (2015), 036402. DOI: 10.1103/PhysRevLett.115.036402.

[53] J. P. Perdew et al. *Periodica Polytechnica. Chemical Engineering; Budapest* **60**, 1 (2016), 2–7. DOI: http://dx.doi.org/10.3311/PPch.8356.

[54] J. Tao and Y. Mo. *Phys. Rev. Lett.* **117**, 7 (2016), 073001. DOI: 10.1103/PhysRevLett.117.073001.

[55] Y. Mo et al. *Phys. Rev. B* **95**, 3 (2017), 035118. DOI: 10.1103/PhysRevB.95.035118.

[56] M. Ernzerhof, J. P. Perdew, and K. Burke. *Int. J. Quantum Chem.* **64**, 3 (1997), 285–295. DOI: 10.1002/(SICI)1097-461X(1997)64:3<285::AID-QUA2>3.0.CO;2-S.

[57] M. Ernzerhof and J. P. Perdew. *J. Chem. Phys.* **109**, 9 (1998), 3313–3320. DOI: 10.1063/1.476928.

[58] A. D. Becke. *J. Chem. Phys.* **98**, 7 (1993), 5648–5652. DOI: 10.1063/1.464913.

[59] J. P. Perdew, M. Ernzerhof, and K. Burke. *J. Chem. Phys.* **105**, 22 (1996), 9982–9985. DOI: 10.1063/1.472933.

[60] K. Burke, M. Ernzerhof, and J. P. Perdew. *J. Chem. Phys. Lett.* **265**, 1–2 (1997), 115–120. DOI: 10.1016/S0009-2614(96)01373-5.

[61] C. Adamo and V. Barone. *J. Chem. Phys.* **110**, 13 (1999), 6158–6170. DOI: 10.1063/1.478522.

[62] J. Paier et al. *J. Chem. Phys.* **124**, 15 (2006), 154709. DOI: 10.1063/1.2187006.

[63] J. Paier et al. *J. Chem. Phys.* **125**, 24 (2006), 249901. DOI: 10.1063/1.2403866.

[64] M. Marsman et al. *J. Phys.: Condens. Matter* **20**, 6 (2008), 064201. DOI: 10.1088/0953-8984/20/6/064201.

[65] N. Seriani et al. *J. Chem. Phys.* **131**, 5 (2009), 054701. DOI: 10.1063/1.3187935.

[66] P. Janthon et al. *J. Chem. Theory Comput.* **10**, 9 (2014), 3832–3839. DOI: 10.1021/ct500532v.

[67] J. Heyd, G. E. Scuseria, and M. Ernzerhof. *J. Chem. Phys.* **118**, 18 (2003), 8207–8215. DOI: 10.1063/1.1564060.

[68] J. Heyd, G. E. Scuseria, and M. Ernzerhof. *J. Chem. Phys.* **124**, 21 (2006), 219906. DOI: 10.1063/1.2204597.

[69] A. V. Krukau et al. *J. Chem. Phys.* **125**, 22 (2006), 224106. DOI: 10.1063/1.2404663.

[70] K. Burke. *J. Chem. Phys.* **136**, 15 (2012), 150901. DOI: 10.1063/1.4704546.

[71] A. J. Cohen, P. Mori-Sánchez, and W. Yang. *J. Chem. Phys.* **129**, 12 (2008), 121104. DOI: 10.1063/1.2987202.

[72] A. J. Cohen, P. Mori-Sánchez, and W. Yang. *Chem. Rev.* **112**, 1 (2012), 289–320. DOI: 10.1021/cr200107z.

[73] M. Fuchs et al. *J. Chem. Phys.* **122**, 9 (2005), 094116. DOI: 10.1063/1.1858371.

[74] S. Grimme and A. Hansen. *Angew. Chem. Int. Ed.* **54**, 42 (2015), 12308–12313. DOI: 10.1002/anie.201501887.

[75] J. P. Perdew, A. Savin, and K. Burke. *Phys. Rev. A* **51**, 6 (1995), 4531–4541. DOI: 10.1103/PhysRevA.51.4531.

[76] J. P. Perdew et al. *J. Chem. Theory Comput.* **5**, 4 (2009), 902–908. DOI: 10.1021/ct800531s.

[77] J. P. Perdew et al. *Phys. Rev. Lett.* **49**, 23 (1982), 1691–1694. DOI: 10.1103/PhysRevLett.49.1691.

[78] Y. Zhang and W. Yang. *J. Chem. Phys.* **109**, 7 (1998), 2604–2608. DOI: 10.1063/1.476859.

[79] B. G. Janesko and G. E. Scuseria. *J. Chem. Phys.* **128**, 24 (2008), 244112. DOI: 10.1063/1.2940738.

[80] S. Lehtola and H. Jónsson. *J. Chem. Theory Comput.* **10**, 12 (2014), 5324–5337. DOI: 10.1021/ct500637x.

[81] E. O. Jónsson, S. Lehtola, and H. Jónsson. *Procedia Comput. Sci.* International Conference On Computational Science, ICCS 2015 **51** (2015), 1858–1864. DOI: 10.1016/j.procs.2015.05.417.

[82] V. I. Anisimov, J. Zaanen, and O. K. Andersen. *Phys. Rev. B* **44**, 3 (1991), 943–954. DOI: 10.1103/PhysRevB.44.943.

[83] M. Cococcioni and S. de Gironcoli. *Phys. Rev. B* **71**, 3 (2005), 035105. DOI: 10.1103/PhysRevB.71.035105.

[84] I. Dabo et al. *Phys. Rev. B* **82**, 11 (2010), 115121. DOI: 10.1103/PhysRevB.82.115121.

[85] B. I. Lundqvist et al. *Int. J. Quantum Chem.* **56**, 4 (1995), 247–255. DOI: 10.1002/qua.560560410.

[86] D. Bohm and D. Pines. *Phys. Rev.* **92**, 3 (1953), 609–625. DOI: 10.1103/PhysRev.92.609.

[87] X. Ren et al. *J. Mater. Sci* **47**, 21 (2012), 7447–7471. DOI: 10.1007/s10853-012-6570-4.

[88] J. J. Mortensen, L. B. Hansen, and K. W. Jacobsen. *Phys. Rev. B* **71**, 3 (2005), 035109. DOI: 10.1103/PhysRevB.71.035109.

[89] J. Enkovaara et al. *J. Phys.: Condens. Matter* **22**, 25 (2010), 253202. DOI: 10.1088/0953-8984/22/25/253202.

[90] F. Bloch. *Z. Physik* **52**, 7-8 (1929), 555–600. DOI: 10.1007/BF01339455.

[91] H. J. Monkhorst and J. D. Pack. *Phys. Rev. B* **13**, 12 (1976), 5188–5192. DOI: 10.1103/PhysRevB.13.5188.

[92] J. D. Pack and H. J. Monkhorst. *Phys. Rev. B* **16**, 4 (1977), 1748–1749. DOI: 10.1103/PhysRevB.16.1748.

[93] M. Plancherel and M. Leffler. *Rend. Circ. Matem. Palermo* **30**, 1 (1910), 289–335. DOI: 10.1007/BF03014877.

[94] C. Rostgaard. *arXiv:0910.1921 [cond-mat, physics:physics]* (2009).

[95] P. E. Blöchl. *Phys. Rev. B* **50**, 24 (1994), 17953–17979. DOI: 10.1103/PhysRevB.50.17953.

[96] G. Kresse and D. Joubert. *Phys. Rev. B* **59**, 3 (1999), 1758–1775. DOI: 10.1103/PhysRevB.59.1758.

[97] M. Marsman and G. Kresse. *J. Chem. Phys.* **125**, 10 (2006), 104101. DOI: 10.1063/1.2338035.

[98] G. Kresse and J. Furthmüller. *Phys. Rev. B* **54**, 16 (1996), 11169–11186. DOI: 10.1103/PhysRevB.54.11169.

[99] I. Chorkendorff and J. W. Niemantsverdriet. *Concepts of Modern Catalysis and Kinetics*. John Wiley & Sons, 2006.

[100] *Drawn with help from the TikZ example 'Clusters of atoms' by A.E. Bolzan.* URL: http://www.texample.net/tikz/examples/clusters-of-atoms/.

[101] K. Siegbahn and C. Nordling. *ESCA, Atomic, Molecular and Solid State Structure Studied by Means of Electron Spectroscopy*. 1967.

[102] S. Mobilio, F. Boscherini, and C. Meneghini, eds. *Synchrotron Radiation - Basics, Methods and Applications*. Springer, 2015.

[103] J. N. Andersen et al. *Phys. Rev. Lett.* **67**, 20 (1991), 2822–2825. DOI: 10.1103/PhysRevLett.67.2822.

[104] E. Lundgren et al. *Phys. Rev. Lett.* **88**, 24 (2002), 246103. DOI: 10.1103/PhysRevLett.88.246103.

[105] M. Todorova et al. *Surf. Sci.* **541**, 1–3 (2003), 101–112. DOI: 10.1016/S0039-6028(03)00873-2.

[106] N. M. Martin et al. *J. Phys. Chem. C* **118**, 28 (2014), 15324–15331. DOI: 10.1021/jp504387p.

[107] G. Onida, L. Reining, and A. Rubio. *Rev. Mod. Phys.* **74**, 2 (2002), 601–659. DOI: 10.1103/RevModPhys.74.601.

[108] L. Hedin. *Phys. Rev.* **139**, 3A (1965), A796–A823. DOI: 10.1103/PhysRev.139.A796.

[109] O. Takahashi and L. G. M. Pettersson. *J. Chem. Phys.* **121**, 21 (2004), 10339–10345. DOI: 10.1063/1.1809610.

[110] D. Nagel. "Interpretation of Valence Bond X-ray Spectra". *Advances in X-ray Analysis*. Vol. 13. New York: Plenum Press, 1970, pp. 182–236.

[111] F. C. Brown. "Ultraviolet Spectroscopy of Solids with the Use of Synchrotron Radiation". *Solid State Physics*. Ed. by F. S. a. D. T. Henry Ehrenreich. Vol. 29. Academic Press, 1974, pp. 1–73.

[112] F. Bechstedt. *Phys. Status Solidi (B)* **112**, 1 (1982), 9–49. DOI: 10.1002/pssb.2221120102.

[113] C. Noguera, D. Spanjaard, and J. Friedel. *J. Phys. F: Met. Phys.* **9**, 6 (1979), 1189. DOI: 10.1088/0305-4608/9/6/022.

[114] E. Pehlke and M. Scheffler. *Phys. Rev. Lett.* **71**, 14 (1993), 2338–2341. DOI: 10.1103/PhysRevLett.71.2338.

[115] J. N. Andersen et al. *Phys. Rev. B* **50**, 23 (1994), 17525–17533. DOI: 10.1103/PhysRevB.50.17525.

[116] A. Pasquarello et al. "Core-Level Shifts in Si(001)-SiO_2 Systems: The Value of First-Principle Investigations". *Fundamental Aspects of Ultrathin Dielectrics on Si-based Devices*. Ed. by E. Garfunkel, E. Gusev, and A. Vul. NATO Science Series 47. Springer Netherlands, 1998, pp. 89–102.

[117] H. Grönbeck et al. *Phys. Rev. B* **85**, 11 (2012), 115445. DOI: 10.1103/PhysRevB.85.115445.

[118] W. L. Jolly and D. N. Hendrickson. *J. Am. Chem. Soc.* **92**, 7 (1970), 1863–1871. DOI: 10.1021/ja00710a012.

[119] W. F. Egelhoff Jr. *Surf. Sci. Rep.* **6**, 6–8 (1987), 253–415. DOI: 10.1016/0167-5729(87)90007-0.

[120] L. Köhler and G. Kresse. *Phys. Rev. B* **70**, 16 (2004), 165405. DOI: 10.1103/PhysRevB.70.165405.

[121] M. Birgersson et al. *Phys. Rev. B* **67**, 4 (2003), 045402. DOI: 10.1103/PhysRevB.67.045402.

[122] H.-P. Komsa, T. T. Rantala, and A. Pasquarello. *Phys. Rev. B* **86**, 4 (2012), 045112. DOI: 10.1103/PhysRevB.86.045112.

[123] K. Siegbahn. *ESCA Applied to Free Molecules*. North-Holland Pub. Co., 1970.

[124] N. D. Lang and A. R. Williams. *Phys. Rev. B* **16**, 6 (1977), 2408–2419. DOI: 10.1103/PhysRevB.16.2408.

[125] A. R. Williams and N. D. Lang. *Phys. Rev. Lett.* **40**, 14 (1978), 954–957. DOI: 10.1103/PhysRevLett.40.954.

[126] D. Spanjaard et al. *Surf. Sci. Rep.* **5**, 1–2 (1985), 1–85. DOI: 10.1016/0167-5729(85)90003-2.

[127] C. Nordling, S. Hagström, and K. Siegbahn. *Z. Physik* **178**, 5 (1964), 433–438. DOI: 10.1007/BF01379472.

[128] M. V. Ganduglia-Pirovano et al. *Phys. Rev. B* **54**, 12 (1996), 8892–8898. DOI: 10.1103/PhysRevB.54.8892.

[129] M. V. Ganduglia-Pirovano, J. Kudrnovský, and M. Scheffler. *Phys. Rev. Lett.* **78**, 9 (1997), 1807–1810. DOI: 10.1103/PhysRevLett.78.1807.

[130] S. Lizzit et al. *Phys. Rev. B* **63**, 20 (2001), 205419. DOI: 10.1103/PhysRevB.63.205419.

[131] V. Nilsson et al. *Surf. Sci.* Reactivity Concepts at Surfaces: Coupling Theory with Experiment **640** (2015), 59–64. DOI: 10.1016/j.susc.2015.03.019.

[132] R. P. Feynman. *Phys. Rev.* **56**, 4 (1939), 340–343. DOI: 10.1103/PhysRev.56.340.

[133] J. D. Head and M. C. Zerner. *J. Chem. Phys. Lett.* **122**, 3 (1985), 264–270. DOI: 10.1016/0009-2614(85)80574-1.

[134] E. Bitzek et al. *Phys. Rev. Lett.* **97**, 17 (2006), 170201. DOI: 10.1103/PhysRevLett.97.170201.

[135] R. Car and M. Parrinello. *Phys. Rev. Lett.* **55**, 22 (1985), 2471–2474. DOI: 10.1103/PhysRevLett.55.2471.

[136] P. Ballone et al. *Phys. Rev. Lett.* **60**, 4 (1988), 271–274. DOI: 10.1103/PhysRevLett.60.271.

[137] D. M. Deaven and K. M. Ho. *Phys. Rev. Lett.* **75**, 2 (1995), 288–291. DOI: 10.1103/PhysRevLett.75.288.

[138] D. J. Wales and J. P. K. Doye. *J. Phys. Chem. A* **101**, 28 (1997), 5111–5116. DOI: 10.1021/jp970984n.

[139] S. Goedecker. *J. Chem. Phys.* **120**, 21 (2004), 9911–9917. DOI: 10.1063/1.1724816.

[140] Y. Wang et al. *Phys. Rev. B* **82**, 9 (2010), 094116. DOI: 10.1103/PhysRevB.82.094116.

[141] D. J. Wales and H. A. Scheraga. *Science* **285**, 5432 (1999), 1368–1372. DOI: 10.1126/science.285.5432.1368.

[142] R. Leardi. *J. Chemometrics* **15**, 7 (2001), 559–569. DOI: 10.1002/cem.651.

[143] R. L. Johnston. *Dalton Trans.* 22 (2003), 4193–4207. DOI: 10.1039/B305686D.

[144] A. R. Oganov, A. O. Lyakhov, and M. Valle. *Acc. Chem. Res.* **44**, 3 (2011), 227–237. DOI: 10.1021/ar1001318.

[145] L. B. Vilhelmsen and B. Hammer. *J. Chem. Phys.* **141**, 4 (2014), 044711. DOI: 10.1063/1.4886337.

[146] S. R. Bahn and K. W. Jacobsen. *Comput. Sci. Eng.* **4**, 3 (2002), 56–66. DOI: 10.1109/5992.998641.

[147] L. D. Lloyd, R. L. Johnston, and S. Salhi. *J. Comput. Chem.* **26**, 10 (2005), 1069–1078. DOI: 10.1002/jcc.20247.

[148] A. O. Lyakhov et al. *Comput. Phys. Commun.* **184**, 4 (2013), 1172–1182. DOI: 10.1016/j.cpc.2012.12.009.

[149] D. Scholl and J. A. Steckel. *Density Functional Theory: A Practical Introduction*. Wiley VCH, 2009.

[150] G. Henkelman, B. Uberuaga, and H. Jónsson. *J. Chem. Phys.* **113**, 22 (2000), 9901–9904. DOI: 10.1063/1.1329672.

[151] G. Henkelman and H. Jónsson. *J. Chem. Phys.* **113**, 22 (2000), 9978–9985. DOI: 10.1063/1.1323224.

[152] D. Sheppard, R. Terrell, and G. Henkelman. *J. Chem. Phys.* **128**, 13 (2008). DOI: 10.1063/1.2841941.

[153] G. Henkelman and H. Jónsson. *J. Chem. Phys.* **111**, 15 (1999), 7010–7022. DOI: 10.1063/1.480097.

[154] A. P. J. Jansen. *An Introduction to Kinetic Monte Carlo Simulations of Surface Reactions*. Vol. 856. Lecture Notes in Physics. 2012.

[155] B. C. Garrett and D. G. Truhlar. "Chapter 5 - Variational Transition State Theory". *Theory and Applications of Computational Chemistry*. Ed. by C. E. Dykstra et al. Amsterdam: Elsevier, 2005, pp. 67–87.

[156] D. G. Truhlar and B. C. Garrett. *Acc. Chem. Res.* **13**, 12 (1980), 440–448. DOI: 10.1021/ar50156a002.

[157] P. Pechukas. "Statistical Approximations in Collision Theory". *Dynamics of Molecular Collisions: Part B*. Ed. by W. H. Miller. Vol. 2. Boston, MA: Springer US, 1976.

[158] H. Eyring. *J. Chem. Phys.* **3**, 2 (1935), 107–115. DOI: 10.1063/1.1749604.

[159] M. G. Evans and M. Polanyi. *Trans. Faraday Soc.* **31**, 0 (1935), 875–894. DOI: 10.1039/TF9353100875.

[160] S. Arrhenius. *Z. Physik. Chem.* **4** (1889), 226.

[161] D. T. Gillespie. *J. Comput. Phys.* **22**, 4 (1976), 403–434. DOI: 10.1016/0021-9991(76)90041-3.

[162] V. P. Zhdanov. *Elementary Physicochemical Processes on Solid Surfaces*. Ed. by M. V. Twigg and M. S. Spencer. Fundamental and Applied Catalysis. Boston, MA: Springer US, 1991.

[163] M. Van den Bossche. "Kinetic Monte Carlo Modeling of the Catalytic Hydrogenation of Benzene on Pt(111)". Master thesis. Ghent University, 2012.

[164] A. Hindmarsh. *IMACS Trans. Sci. Comput.* **1** (1983), 55–64.

[165] A. Hellman and K. Honkala. *J. Chem. Phys.* **127**, 19 (2007), 194704. DOI: 10.1063/1.2790885.

[166] K. Honkala et al. *Science* **307**, 5709 (2005), 555–558. DOI: 10.1126/science.1106435.

[167] A. Hellman et al. *Surf. Sci.* Berlin, Germany: 4–9 September 2005 Proceedings of the 23th European Conference on Surface Science **600**, 18 (2006), 4264–4268. DOI: 10.1016/j.susc.2005.11.070.

[168] J. Berzelius. *Jahres-Bericht* **4** (1823), 60–61.

[169] P. Collins. *Platinum Metals Rev.* **30**, 3 (1986), 141–146.

[170] W. Z. Ostwald. *Z. Physik. Chem.* **15** (1894), 705–706.

[171] S. T. Oyama and G. A. Somorjai. *J. Chem. Educ.* **65**, 9 (1988), 765. DOI: 10.1021/ed065p765.

[172] G. Ertl et al., eds. *Handbook of Heterogeneous Catalysis*. 1st ed. John Wiley & Sons, Inc., 1997.

[173] W. Keim. "Industrial Aspects of Selectivity Applying Homogeneous Catalysis". *Metal Promoted Selectivity in Organic Synthesis*. Ed. by A. F. Noels, M. Graziani, and A. J. Hubert. Catalysis by Metal Complexes 12. Springer Netherlands, 1991, pp. 1–15.

[174] K. J. Laidler. *Pure Appl. Chem.* **68**, 1 (1996), 149–192. DOI: 10.1351/pac199668010149.

[175] D. Eley and E. Rideal. *Nature* **146**, 3699 (1940), 401–402. DOI: 10.1038/146401d0.

[176] P. Mars and D. W. van Krevelen. *Chem. Eng. Sci.* The Proceedings of the Conference on Oxidation Processes **3, Suppl. 1** (1954), 41–59. DOI: 10.1016/S0009-2509(54)80005-4.

[177] C. Stegelmann, A. Andreasen, and C. T. Campbell. *J. Am. Chem. Soc.* **131**, 23 (2009), 8077–8082. DOI: 10.1021/ja9000097.

[178] R. Burch, D. Crittle, and M. Hayes. *Catal. Today* **47**, 1–4 (1999), 229–234. DOI: 10.1016/S0920-5861(98)00303-4.

[179] P. Berlowitz, C. Peden, and D. Goodman. *J. Phys. Chem.* **92**, 18 (1988), 5213–5221. DOI: 10.1021/j100329a030.

[180] K. Fukui, T. Yonezawa, and H. Shingu. *J. Chem. Phys.* **20**, 4 (1952), 722–725. DOI: 10.1063/1.1700523.

[181] J. D. Bradley and G. C. Gerrans. *J. Chem. Educ.* **50**, 7 (1973), 463. DOI: 10.1021/ed050p463.

[182] R. Hoffmann. *Rev. Mod. Phys.* **60**, 3 (1988), 601–628. DOI: 10.1103/RevModPhys.60.601.

[183] G. Blyholder. *J. Phys. Chem.* **68**, 10 (1964), 2772–2777. DOI: 10.1021/j100792a006.

[184] R. Hoffmann. *Angew. Chem. Int. Ed. Engl.* **26**, 9 (1987), 846–878. DOI: 10.1002/anie.198708461.

[185] J. K. Nørskov. *Rep. Prog. Phys.* **53**, 10 (1990), 1253. DOI: 10.1088/0034-4885/53/10/001.

[186] B. Hammer and J. K. Nørskov. "Theoretical Surface Science and Catalysis – Calculations and Concepts". *Advances in Catalysis*. Ed. by H. K. Bruce C. Gates. Vol. 45. Impact of Surface Science on Catalysis. Academic Press, 2000, pp. 71–129.

[187] P. W. Anderson. *Phys. Rev.* **124**, 1 (1961), 41–53. DOI: 10.1103/PhysRev.124.41.

[188] D. M. Newns. *Phys. Rev.* **178**, 3 (1969), 1123–1135. DOI: 10.1103/PhysRev.178.1123.

[189] A. Nilsson and L. G. M. Pettersson. "Chemical Bonding on Metal Surfaces". *Model Systems in Catalysis*. Ed. by R. Rioux. Springer New York, 2010, pp. 253–274.

[190] L. G. M. Pettersson and A. Nilsson. *Top. Catal.* **57**, 1-4 (2014), 2–13. DOI: 10.1007/s11244-013-0157-4.

[191] A. Föhlisch et al. *Phys. Rev. Lett.* **85**, 15 (2000), 3309–3312. DOI: 10.1103/PhysRevLett.85.3309.

[192] H. H. Jaffé and M. Orchin. *Tetrahedron* **10**, 3–4 (1960), 212–214. DOI: 10.1016/S0040-4020(01)97808-1.

[193] H. Jian-Wei et al. *Surf. Sci.* **261**, 1–3 (1992), 164–170. DOI: 10.1016/0039-6028(92)90228-X.

[194] D. Fernández-Torre et al. *J. Chem. Phys.* **141**, 1 (2014), 014703. DOI: 10.1063/1.4885546.

[195] H. Falsig et al. *Angew. Chem.* **120**, 26 (2008), 4913–4917. DOI: 10.1002/ange.200801479.

[196] C. A. Wolcott et al. *J. Catal.* **330** (2015), 197–207. DOI: 10.1016/j.jcat.2015.07.015.

[197] J. K. Nørskov et al. *Nat Chem* **1**, 1 (2009), 37–46. DOI: 10.1038/nchem.121.

[198] F. Abild-Pedersen et al. *Phys. Rev. Lett.* **99**, 1 (2007), 016105. DOI: 10.1103/PhysRevLett.99.016105.

[199] J. Greeley. *Annu. Rev. Chem. Biomol. Eng.* **7**, 1 (2016), 605–635. DOI: 10.1146/annurev-chembioeng-080615-034413.

[200] M. T. M. Koper. *J. Electroanal. Chem.* **660**, 2 (2011), 254–260. DOI: 10.1016/j.jelechem.2010.10.004.

[201] M. Busch et al. *Nano Energy.* Electrocatalysis **29** (2016), 126–135. DOI: 10.1016/j.nanoen.2016.04.011.

[202] A. A. Latimer et al. *Nat. Mater.* **16**, 2 (2017), 225–229. DOI: 10.1038/nmat4760.

[203] G. Kumar et al. *ACS Catal.* **6**, 3 (2016), 1812–1821. DOI: 10.1021/acscatal.5b02657.

[204] A. Latimer et al. *Phys. Chem. Chem. Phys.* **19**, 5 (2017), 3575–3581. DOI: 10.1039/C6CP08003K.

[205] A. Trinchero, A. Hellman, and H. Grönbeck. *Phys. Status Solidi RRL* **8**, 6 (2014), 605–609. DOI: 10.1002/pssr.201409090.

[206] A. Hellman et al. *J. Phys. Chem. Lett.* **3**, 6 (2012), 678–682. DOI: 10.1021/jz300069s.

[207] D. A. Pittam and G. Pilcher. *J. Chem. Soc., Faraday Trans. 1* **68**, 0 (1972), 2224–2229. DOI: 10.1039/F19726802224.

[208] W. P. Yant and C. O. Hawk. *J. Am. Chem. Soc.* **49**, 6 (1927), 1454–1460. DOI: 10.1021/ja01405a010.

[209] J. G. E. Cohn, J. A. J. Haley, and H. C. Andersen. "Method of Effecting the Catalytic Contact of Gases Containing Oxygen and Methane". Pat. US3056646 A. 1962.

[210] R. B. Anderson et al. *Ind. Eng. Chem.* **53**, 10 (1961), 809–812. DOI: 10.1021/ie50622a024.

[211] S. K. Matam et al. *J. Phys. Chem. C* **114**, 20 (2010), 9439–9443. DOI: 10.1021/jp1019697.

[212] G. Zhu et al. *J. Phys. Chem. B* **109**, 6 (2005), 2331–2337. DOI: 10.1021/jp0488665.

[213] J. Rogal, K. Reuter, and M. Scheffler. *Phys. Rev. B* **69**, 7 (2004), 075421. DOI: 10.1103/PhysRevB.69.075421.

[214] J. R. McBride, K. C. Hass, and W. H. Weber. *Phys. Rev. B* **44**, 10 (1991), 5016–5028. DOI: 10.1103/PhysRevB.44.5016.

[215] E. Lundgren et al. *Phys. Rev. Lett.* **92**, 4 (2004), 046101. DOI: 10.1103/PhysRevLett.92.046101.

[216] A. Stierle et al. *J. Chem. Phys.* **122**, 4 (2005), 044706. DOI: 10.1063/1.1834491.

[217] S. Penner et al. *J. Chem. Phys.* **125**, 9 (2006), 094703. DOI: 10.1063/1.2338028.

[218] R. Westerström et al. *Phys. Rev. B* **83**, 11 (2011), 115440. DOI: 10.1103/PhysRevB.83.115440.

[219] H. H. Kan and J. F. Weaver. *Surf. Sci.* **602**, 9 (2008), L53–L57. DOI: 10.1016/j.susc.2008.03.007.

[220] H. H. Kan and J. F. Weaver. *Surf. Sci.* **603**, 17 (2009), 2671–2682. DOI: 10.1016/j.susc.2009.06.023.

[221] K. Momma and F. Izumi. *J. Appl. Crystallogr.* **44**, 6 (2011), 1272–1276. DOI: 10.1107/S0021889811038970.

[222] M. Blanco-Rey and S. J. Jenkins. *J. Chem. Phys.* **130**, 1 (2009), 014705. DOI: 10.1063/1.3046683.

[223] J. F. Weaver et al. *J. Chem. Phys.* **132**, 2 (2010), 024709. DOI: 10.1063/1.3277672.

[224] A. Antony, A. Asthagiri, and J. F. Weaver. *J. Chem. Phys.* **139**, 10 (2013), 104702. DOI: 10.1063/1.4819909.

[225] J. F. Weaver. *Chem. Rev.* **113**, 6 (2013), 4164–4215. DOI: 10.1021/cr300323w.

[226] H. H. Kan et al. *J. Phys. Chem. C* **113**, 4 (2009), 1495–1506. DOI: 10.1021/jp808008k.

[227] J. T. Hirvi et al. *J. Chem. Phys.* **133**, 8 (2010), 084704. DOI: 10.1063/1.3464481.

[228] J. A. Hinojosa, H. H. Kan, and J. F. Weaver. *J. Phys. Chem. C* **112**, 22 (2008), 8324–8331. DOI: 10.1021/jp800216x.

[229] J. A. Hinojosa et al. *J. Phys. Chem. C* **116**, 4 (2012), 3007–3016. DOI: 10.1021/jp2104243.

[230] J. F. Weaver, S. P. Devarajan, and C. Hakanoglu. *J. Phys. Chem. C* **113**, 22 (2009), 9773–9782. DOI: 10.1021/jp9013114.

[231] J. F. Weaver et al. *Catal. Today* **160**, 1 (2011), 213–227. DOI: 10.1016/j.cattod.2010.06.012.

[232] A. Antony et al. *J. Chem. Phys.* **136**, 5 (2012), 054702. DOI: 10.1063/1.3679167.

[233] F. Zhang et al. *Surf. Sci.* **617** (2013), 249–255. DOI: 10.1016/j.susc.2013.07.022.

[234] R. S Monteiro et al. *J. Catal.* **199**, 2 (2001), 291–301. DOI: 10.1006/jcat.2001.3176.

[235] W. F. Schneider et al. *J. Phys. Chem. B* **106**, 30 (2002), 7405–7413. DOI: 10.1021/jp0257496.

[236] H. Grönbeck, P. Broqvist, and I. Panas. *Surf. Sci.* **600**, 2 (2006), 403–408. DOI: 10.1016/j.susc.2005.10.047.

[237] H. Jaffe. *Crystal Chemistry and Refractivity*. Cambridge Earth Science series. Cambridge: Cambridge University Press, 1988.

[238] G. L. Christensen and M. A. Langell. *J. Phys. Chem. C* **117**, 14 (2013), 7039–7049. DOI: 10.1021/jp310344r.

[239] L. Yang et al. *Appl. Catal. B Environ.* **38**, 2 (2002), 117–125. DOI: 10.1016/S0926-3373(02)00034-6.

[240] K. Persson, K. Jansson, and S. G. Järås. *J. Catal.* **245**, 2 (2007), 401–414. DOI: 10.1016/j.jcat.2006.10.029.

[241] N. M. Martin et al. *J. Phys. Chem. C* **120**, 49 (2016), 28009–28020. DOI: 10.1021/acs.jpcc.6b09223.

[242] F. F. Tao et al. *Nat. Commun.* **6** (2015), 7798. DOI: 10.1038/ncomms8798.

[243] H. Okamoto and T. Asô. *Jpn. J. Appl. Phys.* **6**, 6 (1967), 779–779. DOI: 10.7567/JJAP.6.779.

[244] P. O. Nilsson. *J. Phys. C: Solid State Phys.* **12**, 7 (1979), 1423. DOI: 10.1088/0022-3719/12/7/030.

[245] K. C. Hass and A. E. Carlsson. *Phys. Rev. B* **46**, 7 (1992), 4246–4249. DOI: 10.1103/PhysRevB.46.4246.

[246] K.-T. Park et al. *Phys. Rev. B* **49**, 7 (1994), 4425–4431. DOI: 10.1103/PhysRevB.49.4425.

[247] S. Grimme et al. *J. Chem. Phys.* **132**, 15 (2010), 154104. DOI: 10.1063/1.3382344.

[248] D. Fernández-Torre et al. *J. Phys. Chem. C* **116**, 25 (2012), 13584–13593. DOI: 10.1021/jp212605g.

[249] T. P. Senftle et al. *J. Chem. Phys.* **139**, 4 (2013), 044109. DOI: 10.1063/1.4815820.

[250] L. B. Vilhelmsen and B. Hammer. *Phys. Rev. Lett.* **108**, 12 (2012), 126101. DOI: 10.1103/PhysRevLett.108.126101.